Investigating the dependence of mineral dust depolarization on complex refractive index and size with a laboratory polarimeter at 180.0° lidar backscattering angle

Alain Miffre[1], Danaël Cholleton[1], Clément Noël[1] and Patrick Rairoux[1]

[1]University of Lyon, Université Claude Bernard Lyon 1, CNRS, Institut Lumière Matière, F-69622, Villeurbanne, France

Correspondence to: Alain Miffre (alain.miffre@univ-lyon1.fr)

Abstract. In this paper, the dependence of the particles depolarization ratio (*PDR*) of mineral dust on the complex refractive index and size is for the first time investigated through a laboratory π-polarimeter operating at 180.0° backscattering angle and at (355, 532) nm wavelengths for lidar purposes. The dust *PDR* is indeed an important input parameter in polarization lidar experiments involving mineral dust. Our π-polarimeter provides sixteen accurate (< 1 %) values of the dust lidar *PDR* at 180.0° corresponding to four different complex refractive indices, studied at two size distributions (fine, coarse) ranging from 10 nm to more than 10 µm, and at (355, 532) nm wavelengths, while accounting for the highly irregular shape of mineral dust, which is difficult to model numerically. At 355 nm, the lidar *PDR* of coarser silica, the main oxide in mineral dust, is equal to (33 ± 1) % while that of coarser hematite, the main light absorbent in mineral dust, is (10 ± 1) %. This huge difference is here explained by accounting for the high imaginary part of the hematite complex refractive index. In turn, Arizona dust exhibits higher depolarization than Asian dust, due to the higher proportion in hematite in the latter. As a result, when the strong light absorbent hematite is involved, the dust lidar *PDR* primarily depends on the particles complex refractive index and its variations with size and shape are less pronounced. When hematite is less or not involved, the dust lidar *PDR* increases with increasing sizes, though the shape dependence may then also play a role. and tThe (355, 532) nm wavelength dependence of the dust lidar *PDR* then allows discussing on the involved particle sizes, thus highlighting the importance of dual-wavelength (or more) polarization lidar instruments. We believe these laboratory findings will help improving our understanding of the challenging dependence of the dust lidar *PDR* with complex refractive index and size to help interpret the complexity and the wealth of polarization lidar signals.

1 Introduction

With worldwide annual emissions between 1000 to 3000 Tg (Monge et al., 2012), mineral dust is a highly important constituent of the atmosphere, which contributes to ice cloud formation by acting as a freezing nucleus and to the carbon cycle by fertilizing nutrient poor ecosystems such as the Amazon rainforest after long-range transport (Bristow et al., 2010). As underscored in the latest IPCC report (2021), mineral dust also contributes to the Earth's radiative budget through light scattering and

30 absorption, by reducing the amount of energy reaching the Earth's surface (Kosmopoulos et al., 2017). The radiative impact

31 associated with a Saharan dust storm has been recently quantified by (Francis et al., (2022). This climatic impact is however

32 subject to large uncertainties, mainly due to the great complexity in size, shape and mineralogy of mineral dust. In the

33 atmosphere, the size distribution of mineral dust is mainly determined by the distance from the dust source region. Two freshly

34 uplifted dust aerosols may indeed exhibit different size distributions at far-range remote sites (Ryder et al., 2013), due to the

35 rapid removal of the largest particles by gravitational settling. Mineral dust particles also exhibit a high degree of complexity

36 in shape. Electron microscopic images (Kandler et al., 2011) indeed highlight the nonspherical and highly irregular shape of

37 mineral dust particles, with sharp edges, sometimes even surface roughness (Nousiainen, 2009). The mineral dust surface is

38 itself subject to photo-catalytic reactions leading even to new particle formation events (Dupart et al., 2012). The third degree

39 of complexity of mineral dust related to this study lies in its mineralogy. Mineral dust indeed consists in a heterogeneous

40 mixture of various chemical oxides among which the most predominant is silica oxide. Aluminum and iron oxides are also

41 present in proportions depending on the dust source region. As an example, the desert in Central Australia is iron oxides rich

42 (Bullard and White, 2002). This diverse mineralogy results in a diversity of complex refractive indices for mineral dust.

43

44 In the atmosphere, mineral dust is additionally often mixed with other aerosols. To face such a complexity, ground and satellite-

45 based polarization lidar instruments, based on light backscattering by nonspherical particles, have been developed

46 (Freudenthaler et al., 2009; Tesche et al., 2009; Sugimoto and Lee, 2006; Winker et al., 2009; Miffre et al., 2019; Hofer et al.,

47 2020; Hu et al., 2020) to discern the mineral dust contribution to two-component particles external mixtures, by applying lidar

48 partitioning algorithms such as the $1\beta + 1\delta$ algorithm (Tesche et al., 2009; Mehri et al., 2018). Such lidar-based retrievals are

49 however under-constrained and depend on prior knowledge regarding input parameters such as the lidar particles'

50 depolarization ratio (PDR). The lidar PDR quantifies the mineral dust particles deviation from isotropy and is key for aerosol

51 typing (Hofer et al., 2020; Burton et al., 2012). As explained in light scattering textbooks (Bohren and Huffman, 1983;

52 Mishchenko et al., 2002), it depends on the particles size, shape and complex refractive index. The size dependence of the

53 lidar PDR was studied in field by (Hofer et al., (2020). The downside of such field measurements is that the observed aerosol

54 is nevertheless that of a particles mixture, which may induce some discrepancies in the retrieved dust lidar PDR (Miffre et al.,

55 2011). As an alternate, for accurate retrievals of the mineral dust lidar PDR, light backscattering numerical simulations have

56 been developed, by assuming a particles shape model such as the spheroidal shape model, computed with the T-matrix

57 numerical code (Mishchenko and Travis, 1998), as successfully applied for mineral dust during the SAMUM field campaign

58 (Müller et al., 2013) or, by considering more realistic shapes, based on stereograms, computed with the discrete-dipole-

59 approximation (Lindqvist et al., 2014; Gasteiger et al., 2011). Depending on the assumed shape model, the lidar PDR can be

60 very different with induced variations in the lidar-retrieved dust mass concentrations (Mehri et al., 2018). Recently, (Luo et

61 al., (2022;) and Huang et al., (2022) discussed on the ability of the spheroidal model to mimic the complex shape of mineral

62 dust. Likewise, (Zubko et al., (2013) found spheroids inadequate for describing the dust particles' spectral dependence of the

63 lidar PDR. Such light scattering numerical simulations nonetheless rely on simplifying assumptions that should be carefully

64 checked. Laboratory experiments on natural dust samples at 180.0° lidar exact backscattering angle are then looked-for as they

65 provide quantitative evaluations of the mineral dust lidar *PDR* within experimental error bars. Indeed, in laboratory, the

66 retrieved lidar *PDR* is, by construction, that of pure mineral dust and the dependence of the dust lidar *PDR* with size and

67 mineralogy can be evaluated. Moreover, the complex shape of mineral dust is then accounted for. However, existing laboratory

68 light scattering experimental set-ups (Glen and Brooks, 2013; Järvinen et al., 2016; Gautam et al., 2020; Liu et al., 2020;

69 Kahnert et al., 2020; Gómez Martín et al., 2021) can only provide approximate values of the dust lidar *PDR* for the following

70 reasons:

71

72   − Such apparatuses operate at near backscattering angles only (< 180.0°), without covering the exact lidar

73   backscattering angle of 180.0°. The retrieved lidar *PDR* is then extrapolated to 180.0° following simplifying

74   numerical assumptions, ignoring the complexity in shape of mineral dust (Liu et al., 2020; Gómez Martín et al., 2021).

75   To provide accurate values of the dust lidar *PDR*, such assumptions must be carefully discussed as the lidar *PDR*

76   actually depends on the scattering angle in an unpredictable way, as underscored in light scattering textbooks (Bohren

77   and Huffman, 1983; Mishchenko et al., 2002), due to the complex shape of mineral dust. For that, a laboratory

78   measurement of the dust lidar *PDR* at 180.0° is mandatory.

79   − Also, most of the above apparatuses operate at a single wavelength, either 442, 488, 552, 632, 647 or 680 nm, which

80   differs from the (355, 532, 1064 nm) wavelengths which are applied in polarization lidar field experiments. As for

81   Raman lidars, such wavelength extrapolations up to the (355, 532, 1064 nm) lidar wavelengths are a source of

82   discrepancy as the dust lidar *PDR* actually depends on the complex refractive index, which is wavelength dependent

83   (Bohren and Huffman, 1983; Mishchenko et al., 2002). For that, a laboratory measurement at the lidar wavelengths

84   is mandatory.

85

86 In this paper, accurate values (< 1%) of the dust lidar *PDR* are provided from a laboratory π-polarimeter operating at 180.0°

87 lidar exact backscattering angle and at 355, 532 nm wavelength, to account for the importance of the spectral dependence of

88 the lidar *PDR* to better constrain lidar inversions and aerosol typing (Burton et al., 2016; Haarig et al., 2022). Since the

89 scattering angle and the wavelengths are determined forfrom lidar purposes, we here investigate the dependence of the mineral

90 dust lidar *PDR* on the dust particles size and complex refractive index (*CRI*), the latter being particularly important as related

91 to light absorption. Light absorption by mineral dust preferentially occurs in the UV and VIS spectral domains, being nearly

92 null in the near-infrared spectral range (Di Biagio et al., 2019), noticeably in the presence of iron oxides (Formenti et al., 2014;

93 Caponi et al., 2017). By absorbing short-wave radiations, such oxides hence play a critical role in determining the overall

94 impact of dust aerosol on climate forcing (Go et al., 2022). We hence focused on 355 and 532 nm lidar wavelengths and

95 considered four dust samples differing in their *CRI*, thus in mineralogy: i) silica oxide (SiO_2), as the most abundant mineral

96 oxide present in mineral dust, ii) iron oxide (hematite, Fe_2O_3), as the main light absorbent present in mineral dust (Gautam et

97 al., 2020; Zong et al., 2021; Go et al., 2022), iii) and iv) two heterogeneous mixtures of the above two oxides in various

98 proportions, as detailed in Section 2. The dependence of the lidar PDR with size is then likewise investigating by accounting

99 for the fine and coarse modes of the particles size distribution (SD), to which lidar instruments are sensitive (Mamouri and

100 Ansmann, 2017), thus extending the size range of our previous laboratory findings (Miffre et al., 2016) to particles sizes larger

101 than 800 nm and to other mineralogy, as asked for in ~~(~~Tesche et al.~~,~~ (2019). According to the manufacturer, the size distribution

102 of our dust samples ranged from 10 nm to more than 10 μm in diameter. Our work provides sixteen laboratory-derived accurate

103 dust lidar PDR values, corresponding to four mineral dust samples differing in mineralogy, given at two SD (fine, coarse) and

104 at two wavelengths (355, 532 nm). Moreover, the role of the imaginary part of the hematite CRI, which may lead to

105 modifications in the lidar PDR, is here for the first time quantified and discussed.

106

107 -The paper is structured as follows. In Section 2, the complex refractive indices and size distributions of our four dust samples

108 are presented. The laboratory π-polarimeter at 180.0° lidar backscattering angle is then presented in Section 3, together with

109 the dust lidar PDR retrieval methodology, derived from the scattering matrix formalism (Mishchenko et al., 2002). The main

110 findings are outlined in Section 4 where the sixteen values of dust lidar PDR are given and a discussion is proposed to

111 investigate the dependence of the dust lidar PDR on the imaginary part of the dust CRI. As in elastic lidar applications, we

112 here consider the elastic backscattering of ~~an~~ electromagnetic radiation of wavelength λ by an ensemble of mineral dust

113 particles of complex refractive index $m = n + i\kappa$ embedded in ambient air.

114 **2. Mineral dust samples**

115 **2.1 Refractive indices**

116 Mineral dust is a complex mixture of several chemical oxides presenting various complex refractive indices. To investigate

117 the dependence of the dust lidar PDR on the complex refractive index (CRI), we consider the four following case studies :

118

119 –   Silica, or silicon oxide (SiO$_2$) is here considered as being the main pure chemical component present in mineral dust.

120   The silica CRI as given by ~~(~~Longtin et al. ~~(~~1988) is equal to 1.546, hence exhibiting no absorptive component.

121 –   Iron oxide, or hematite (Fe$_2$O$_3$), is in contrast here selected as being a climatically significant light absorbent in the

122   shortwave spectral region, that can be transported far from source regions with similar efficiency as black carbon

123   particles (Lamb et al., 2021). It recently regained in interest with papers specifically dedicated to this constituent

124   (Gautam et al., 2020; Zong et al., 2021). Hematite is unique among all chemical oxides present in mineral dust due

125   its strong CRI. Both n and κ are large for hematite, with κ-values more than 100 times those of other soil mineral

126   components at lidar wavelengths. Hence, hematite dominates absorption while other minerals can be considered as

127   non-absorbing (Go et al., 2022). ~~Reference literature for the hematite CRI is $m = 3.102 + 0.0925i$ by (Longtin et~~

4

128 ~~al., 1988). More recently,~~ The real and imaginary part of the hematite CRI is provided by ~~(~~Scanza et al.~~,~~ (2015)~~: $m =$~~
129 ~~$2.13 + 0.94i$ at 355 nm wavelength ($3.07 + 0.55i$ at 532 nm wavelength).~~the real and imaginary part of the hematite
130 ~~CRI were reviewed by (Go et al., 2022): from their Figure 1, we conclude that $m = 2.25 + 0.9i$ at 355 nm wavelength~~
131 ~~($m = 3.10 + 0.6i$ at 532 nm wavelength)~~.

132 – Arizona ~~Test dust~~ Dust (hereafter called Arizona dust) is likewise considered as an example of natural mineral dust
133 sample that is ~~involving~~ a mixture of the above two oxides. According to the manufacturer (Power Technology Inc.),
134 Arizona Test Dust is composed of silica (68-76 %), while hematite is only weakly present in Arizona dust (2-5 %).
135 In short, Arizona dust is hence rather silica-rich. As given by the manufacturer, the Arizona dust CRI is $m = 1.51 +$
136 $10^{-3}i$, without however any given on its spectral dependency. Effective medium theories can alternately be applied
137 to account for the sample inhomogeneity as calculated in ~~(~~Miffre et al.~~,~~ (2016), who arrived to $m = 1.57 + 10^{-2}i$ at
138 355 nm wavelength and $1.55 + 5.10^{-3}i$ at 532 nm wavelength. As a result, the Arizona dust sample CRI is
139 characterized by $n \sim 1.5$ and a low absorbing component $\kappa \sim 5.10^{-3}$.

140 – Asian dust is finally also considered as an important case study of natural mineral dust sample, presenting however a
141 lower proportion of silica (34-40 %) and a higher proportion in hematite (17-23 %). For Asian dust, we use a
142 commercial sample provided by Powder Technology (commercial name: Kanto Loam), commonly used as a dust
143 interferon in pollen light scattering measurements in Japan (Iwai, 2013), hence representative of observed atmospheric
144 Asian dust. In this way, we symmetrized our approach by dealing with both Arizona Test Dust and Asian Test Dust.
145 The CRI of Asian dust, evaluated from effective medium approximation, is m = 1.70 + 0.09i at 355 nm wavelength
146 and 1.72 + 0.03i at 532 nm wavelength. Hence, compared with Arizona dust, Asian dust is more hematite-rich and
147 hence exhibits a larger imaginary part for its CRI.

148

149 Other chemical oxides are also present in our dust samples in various percentages, but with negligible imaginary parts of CRI
150 compared with that of hematite. Investigating the PDR of these oxides is then beyond the scope of this paper. Their percentage
151 in (Arizona Test Dust, Asian Dust) is given for clarity: Al_2O_3 (11 %, 29 %), CaO (4 %, 1.5 %), K_2O (3.5 %, 0 %), Na_2O (2 %,
152 0 %), MgO (1.5 %, 5 %), TiO_2 (0.5 %, 2 %). The solid dust samples, provided by Sigma Aldrich and Powder Technology
153 manufacturers, were embedded in laboratory ambient air by using a solid dust generator supplied with dried compressed air
154 ($RH < 10$ %) to get dry solid dust particles embedded in laboratory ambient air at a constant number concentration, before
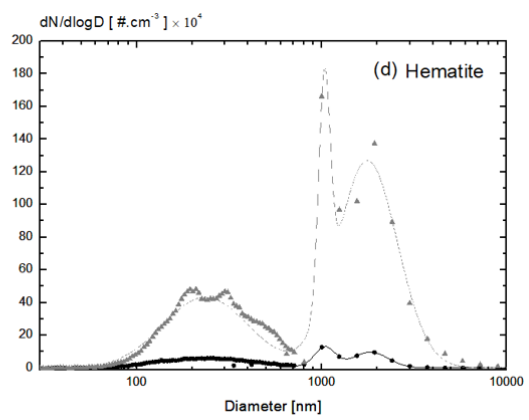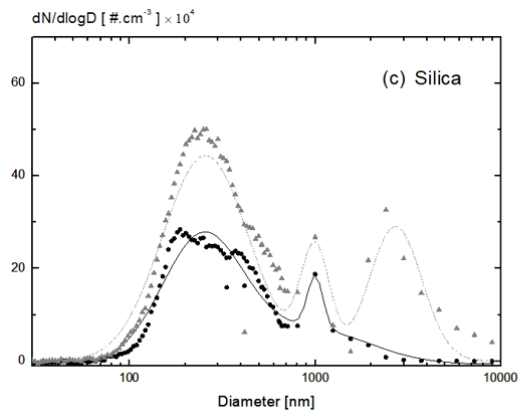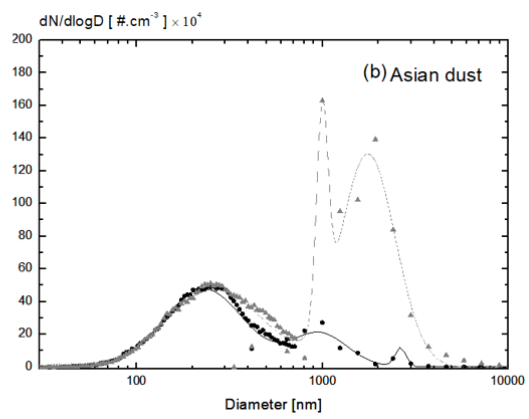155 injecting the dust samples into the light scattering volume, as presented in Section 3.
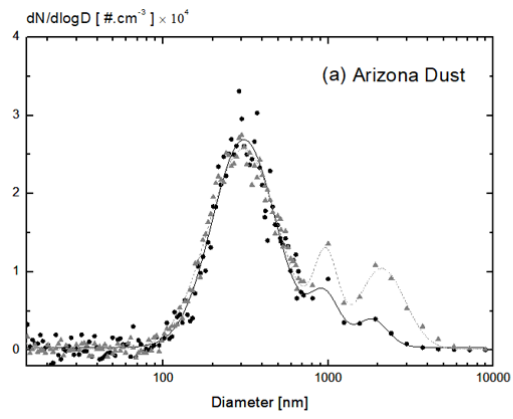
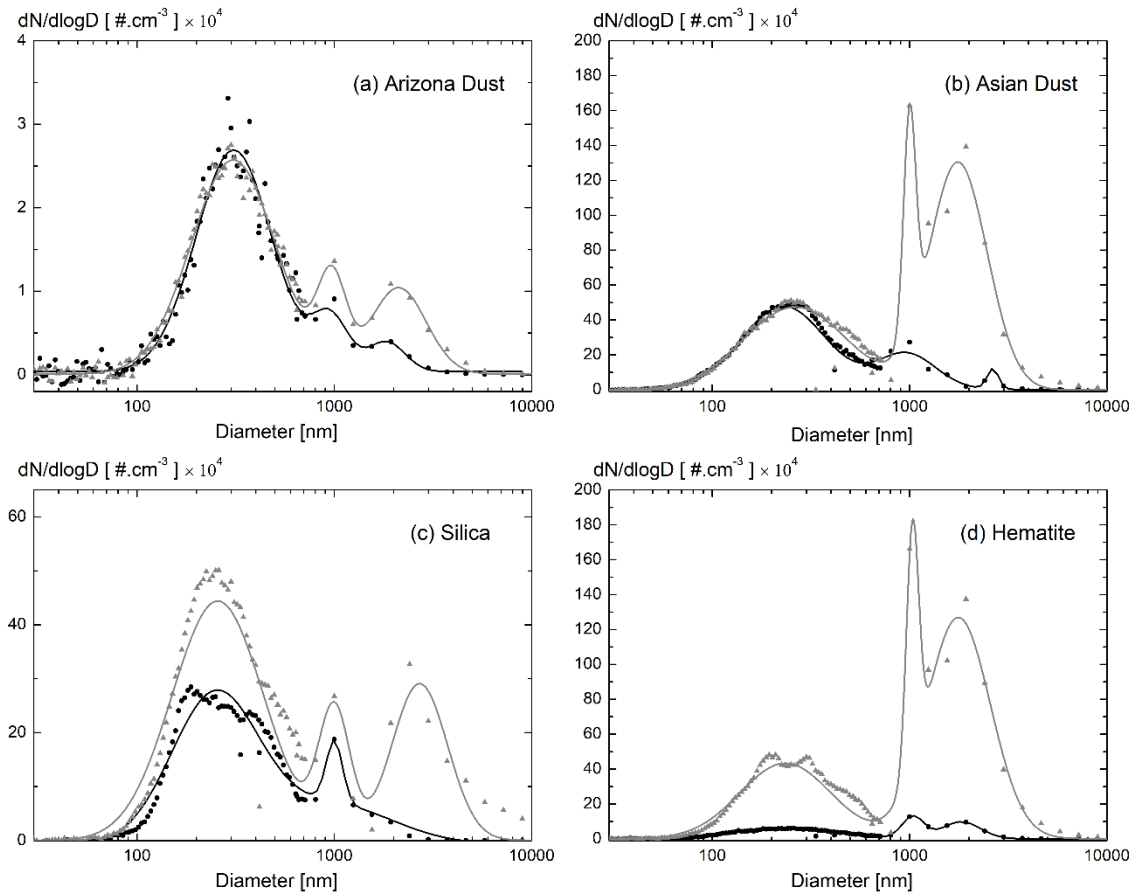156 **2.2 Size distribution (SD)**

157 For each above dust sample, ~~to likewise investigate the dependence of the dust lidar PDR on the particles size,~~ we consider
158 two size distributions (SD)~~:~~. to likewise investigate the dependence of the dust lidar PDR on the particles size:

5

159   –   The coarser *SD*, represented in grey in ~~Figure~~ Fig. 1. This SD is more representative of mineral dust particles close

160   to dust regions, although it does not cover the full range of large dust particles measured close to dust sources, showing

161   particles with diameters > 50 μm (Ryder et al., 2019)~~This *SD* is aimed at being more representative of mineral dust~~

162   ~~particles close to dust source regions~~,

163   –   A finer *SD*, plotted with ~~represented in~~ a black line in ~~Figure~~ Fig. 1, aimed at being more representative of mineral

164   dust particles after long-range transport, i.e. farther from the dust source regions.

165 The *SD* were obtained by adding / removing a cyclone to our experimental set-up allowing to add / remove particles with

166 diameter above 800 nm, thus exploring particles size ranges below and above 800 nm, as asked for in ~~(~~Tesche et al.~~,~~ (2019).

167 More precisely, the two considered SD correspond to a size distribution with and without coarse mode. The *SD* were measured

168 with an optical particles sizer (OPS 3330) coupled with a scanning mobility particles sizer (SMPS 3081), which selects the

169 dust particles as a function of their electric mobility, this latter quantity being diameter-dependent. As in ~~(~~Järvinen et al.~~,~~

170 (2016), our size instruments could not measure dust particles with diameter above 10 μm. According to the manufacturer, such

171 giant particles (Ryder et al., 2019) are however present in our dust samples, at a low number concentration. The measured SD

172 are representative of what is observed in atmosphere, with a low number concentration of more than 10 μm particles, as

173 observed by ~~(~~Weinzierl et al.~~,~~ (2017). The particles *SD* displayed in ~~Figure~~ Fig. 1 are in agreement with the specifications

174 provided by the manufacturers.

175

dN/dlogD [#.cm⁻³] × 10⁴ — (a) Arizona Dust, Diameter [nm]

dN/dlogD [#.cm⁻³] × 10⁴ — (b) Asian dust, Diameter [nm]

dN/dlogD [#.cm⁻³] × 10⁴ — (c) Silica, Diameter [nm]

dN/dlogD [#.cm⁻³] × 10⁴ — (d) Hematite, Diameter [nm]

176

7

Figure 1: Dust particles size distributions (SD) for: (a) Arizona dust, (b) Asian dust, (c) Silica (SiO_2), (d) Hematite (Fe_2O_3) in the presence / absence of the added cyclone (finer SD, in solid black) / (coarser SD, in dotted grey). The retrieved SD, obtained by log-normal adjustments, agree with the specifications provided by the manufacturers.

3 Methodology

In this section, we detail our methodology for accurate laboratory evaluations of the dust lidar PDR at lidar exact backscattering angle of 180.0° for accurate lidar PDR-retrievals.

3.1 Scattering matrix formalism

The dust lidar PDR can be evaluated in the framework of the scattering matrix formalism ~~, which is the dedicated formalism for polarization resolved elastic light scattering measurements, as recommended in light scattering textbooks~~ (Mishchenko et al., 2002; Bohren and Huffman, 1983). In this formalism, the polarization state of the incident and scattered radiations are described by their respective Stokes vectors $\boldsymbol{St_i} = [I_i, Q_i, U_i, V_i]^{\mathrm{T}}$ and $\boldsymbol{St} = [I, Q, U, V]^{\mathrm{T}}$, defined with respect to the scattering plane, used as a reference plane (Mishchenko et al., 2002). The first Stokes component I corresponds to the light intensity, Q

8

190 and U describe linear polarization, while V accounts for circular polarization. At a distance d from the mineral dust samples,
191 if single-scattering and particles random orientation are assumed, <u>for macroscopically isotropic and mirror-symmetric</u>
192 <u>mediums,</u> the incident and scattered Stokes vectors relate with a bloc-diagonal scattering matrix (Mishchenko et al., 2002;
193 Bohren and Huffman, 1983):

194

195
$$\begin{pmatrix} I \\ Q \\ U \\ V \end{pmatrix} = \frac{1}{k^2 d^2} \begin{bmatrix} F_{11,\lambda}(\theta) & F_{12,\lambda}(\theta) & 0 & 0 \\ F_{12,\lambda}(\theta) & F_{22,\lambda}(\theta) & 0 & 0 \\ 0 & 0 & F_{33,\lambda}(\theta) & F_{34,\lambda}(\theta) \\ 0 & 0 & -F_{34,\lambda}(\theta) & F_{44,\lambda}(\theta) \end{bmatrix} \begin{pmatrix} I_i \\ Q_i \\ U_i \\ V_i \end{pmatrix}$$
(1)

196

197 Where the matrix elements $F_{ij,\lambda}(\theta)$ $(i,j = 1-4)$ depend on the wavelength λ of the radiation (hereafter noted as a subscript)
198 and ~~comprise the~~<u>carry</u> information on the mineral dust particles size, shape and CRI. The scattering angle is $\theta = (\boldsymbol{k_i}, \boldsymbol{k})$, where
199 $k = k_i = 2\pi/\lambda$ is the wave vector of the <u>electromagnetic wave</u>~~radiation~~. In lidar applications, the scattering angle is equal to
200 π (i.e. exact backscattering angle). To highlight the need for laboratory measurements at the specific 180.0° lidar
201 backscattering angle, near backscattering angles (i.e. $\theta < \pi$) are also considered in this section. Indeed, at ~~specific lidar~~
202 ~~backscattering angle (~~$\theta = \pi$~~)~~, $F_{33,\lambda} = -F_{22,\lambda}$ and $F_{12,\lambda} = F_{34,\lambda} = 0$ (Zubko et al., 2013; David et al., 2013) while $F_{44,\lambda} =$
203 $F_{11,\lambda} - 2F_{22,\lambda}$ due to the backscattering theorem (van de Hulst, 1957), so that Eq. (1) simplifies as follows for lidar
204 applications:

205

206
$$\begin{pmatrix} I \\ Q \\ U \\ V \end{pmatrix} = \frac{1}{k^2 d^2} \begin{bmatrix} F_{11,\lambda}(\pi) & 0 & 0 & 0 \\ 0 & F_{22,\lambda}(\pi) & 0 & 0 \\ 0 & 0 & -F_{22,\lambda}(\pi) & 0 \\ 0 & 0 & 0 & F_{11,\lambda}(\pi) - 2F_{22,\lambda}(\pi) \end{bmatrix} \begin{pmatrix} I_i \\ Q_i \\ U_i \\ V_i \end{pmatrix}$$
(2)

207

208 As a result, it is only at elastic lidar exact backscattering angle ($\theta = \pi$) that $F_{12,\lambda} = 0$ so that the scattering matrix reduces to
209 only two non-vanishing elements $F_{11,\lambda}(\pi)$ and $F_{22,\lambda}(\pi)$.

210 **3.2 Lidar particles depolarization ratio PDR**

211 The expression of the so-called particles <u>linear</u> depolarization ratio (PDR) at wavelength λ and scattering angle θ can be
212 found in light scattering textbooks (Mishchenko et al., 2002; Schnaiter et al., 2012):

213

214
$$PDR_\lambda(\theta) = \frac{1 - F_{22,\lambda}(\theta)/F_{11,\lambda}(\theta)}{1 \pm 2F_{12,\lambda}(\theta)/F_{11,\lambda}(\theta) + F_{22,\lambda}(\theta)/F_{11,\lambda}(\theta)}$$
(3)

215

216 where the positive (resp. negative) sign corresponds to p-polarized (resp. s-polarized) incident electromagnetic radiation. The

217 PDR stated in Eq. (3) is the linear PDR, which can be related to the circular PDR if need be (Mishchenko et al., 2002). ~~For~~

218 ~~$F_{11,\lambda}$, $F_{12,\lambda}$ and $F_{22,\lambda}$ vary with the scattering angle θ, so does the dust PDR.~~ Since $F_{11,\lambda}$, $F_{12,\lambda}$ and $F_{22,\lambda}$ may vary with the

219 scattering angle, depending on the dust sample, the dust PDR at near backscattering angles ($\theta < \pi$) differs from that obtained

220 at specific lidar backscattering angle ($\theta = \pi$). The deviation of $F_{11,\lambda}$, $F_{12,\lambda}$ and $F_{22,\lambda}$ from their value at exact backscattering

221 angle cannot be quantified since no analytical light scattering theory exists for such complex-shaped particles as mineral dust.

222 Therefore, a laboratory experiment at specific lidar exact backscattering angle ($\theta = \pi$) is required for precise evaluations of

223 the dust lidar PDR. At specific lidar backscattering angle of π, Eq. (3) becomes:

224

225 $$PDR_\lambda(\pi) = \frac{1 - F_{22,\lambda}(\pi)/ F_{11,\lambda}(\pi)}{1 + F_{22,\lambda}(\pi)/ F_{11,\lambda}(\pi)} \qquad\qquad (4)$$

226

227 Hence ~~and as a result~~, accurate evaluations of the dust lidar PDR rely on accurate determinations of the ratio $F_{22,\lambda}/F_{11,\lambda}$ at

228 specific lidar $\pi -$ angle. As for the ratio $F_{22,\lambda}/F_{11,\lambda}$, the dust lidar PDR is size, shape and refractive index dependent and this

229 dependency is discussed in Section 4. Spherical particles, for which $F_{22,\lambda}/F_{11,\lambda} = 1$, lead to $PDR_\lambda(\pi) = 0$~~zero depolarization~~.

230 In what follows, to ease the reading, the dust lidar PDR will be noted PDR_λ without reference to scattering angle ($\theta = \pi$).

231 **3.3 Laboratory π-polarimeter for retrieving the lidar PDR of mineral dust**

232 In (Miffre et al., 2016), for the first time to our knowledge, a laboratory π-polarimeter was built to address light

233 backscattering by aerosol particles. We here recall its main characteristics for clarity. The aerosols π-polarimeter is schemed

234 in ~~Figure~~ Fig. 2. As in lidar applications, pulsed laser light is used to measure the time-of-flight taken by a laser pulse to reach

235 the dust sample and be detected after light backscattering. The backscattering geometry is set by inserting a ~~specified~~ well-

236 characterized ~~polarization~~ polarizing beam splitter cube (PBC) ~~on the way from the laser pulse to the dust samples~~between the

237 emission and the dust samples, with a precision of 1 mm out of 10 meters to ensure the π-polarimeter ~~to cover~~covers the lidar

238 exact backscattering direction with accuracy: $\theta = (180.0 \pm 0.2)°$. The laboratory aerosol π~~Pi~~-polarimeter is actually

239 composed of two identical polarimeters, one per wavelength, to evaluate the lidar PDR of a given dust sample at 355 and 532

240 nm wavelength simultaneously. Moreover, to ~~gain in accuracy~~decrease the retrieval uncertainty on ~~in~~ the dust ~~lidar~~ PDR ~~-~~

241 ~~retrieval~~, the polarization state of the backscattered radiation is analysed for a set of incident polarization states~~, obtained by~~

242 ~~modulating~~ of the incident ~~polarization state~~light using ~~with~~a quarter-wave plate (QWP). To validate the laboratory π-

243 polarimeter, we carefully checked that homogeneous spherical particles, such as ammonium sulfate particles, which scatter

244 light as described by ~~follow~~the Mie theory (Bohren and Huffmann, 1983), were indeed providing zero lidar PDR when

245 following the methodology described in the below section.

246
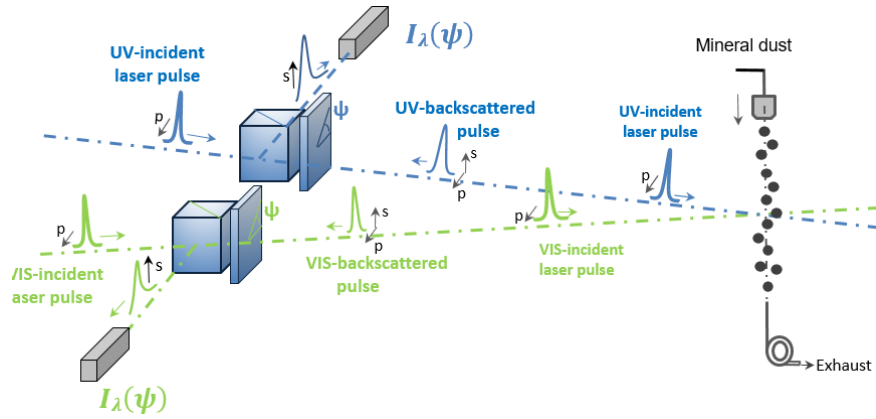
247

248 Figure 2: Scheme of the laboratory π-polarimeter operating at lidar exact backscattering angle of $(180.0 \pm 0.2)°$ allowing accurate retrievals
249 of the lidar PDR at 355 and 532 nm wavelength simultaneously for ~~of~~ an aerosol sample (Miffre et al., 2016)~~at 355 and 532 nm wavelength~~
250 ~~simultaneously (Mishchenko et al., 2002)~~. The (p, s) polarization components are defined with respect to the laser scattering plane and ψ is
251 the angle between the fast axis of the QWP and the laser scattering plane, counted counter-clockwise for an observer looking from the PBC
252 to the particles. The dust lidar PDR is then evaluated from the ratio $F_{22,\lambda}/F_{11,\lambda}$ at specific π-angle, following the methodology described in
253 Section 3.4.

254 **3.4 Laboratory retrievals of mineral dust PDR**

255 ~~Interestingly, the laboratory π-polarimeter can be described in the framework of the scattering matrix formalism~~We can
256 formulate the PDR measurements of dust particles, using ~~(Mishchenko et al., 2002). Hence, to retrieve the dust PDR, we~~
257 ~~account for the~~ successive Mueller matrices denoting to the optical elements of the π-polarimeter and the scattering medium,
258 encountered by the laser pulse from the laser source to the dust particles sample then back to the light detector. The measured
259 ~~to get the expression of the the detected~~ backscattered intensity is :

260

261 $I_\lambda(\psi) = \frac{\eta_\lambda P_\lambda}{d^2} [1, 0, 0, 0]^T [\boldsymbol{PBC}][\boldsymbol{QWP}(-\psi)][\boldsymbol{F_\lambda}][\boldsymbol{QWP}(\psi)][\boldsymbol{PBC}](St_i)$ (5)

262

263 Where η_λ is the optoelectronics efficiency of the~~our~~ light detector and P_λ is the laser power density, while $(St_i) =$
264 $[1, 1, 0, 0]^T$ is~~et~~s the Stokes vector of the ~~laser~~-incident laser light~~polarization state~~. The expression of the dust backscattering
265 matrix $[\boldsymbol{F_\lambda}]$ at wavelength λ is is given in Eq. (2), while $[\boldsymbol{PBC}]$ and $[\boldsymbol{QWP}(\pm\psi)]$ are the Mueller matrices of the PBC and the
266 QWP respectively (Shurcliff, 1962). To develop Eq. (5), it is then advised to first calculate the raw vector
267 $[1, 0, 0, 0]^T [\boldsymbol{PBC}][\boldsymbol{QWP}(-\psi)][\boldsymbol{F_\lambda}]$ then multiply it with the Stokes vector of the ~~radiation~~ incident laser light
268 $[\boldsymbol{QWP}(\psi)][\boldsymbol{PBC}](St_i)$ equal to $[1, \cos^2(2\psi), -\sin(4\psi)/2, -\sin(2\psi)]^T$, with~~if~~ ψ ~~is~~ the modulation angle of the QWP. After
269 a few calculations, the dust backscattered light intensity I_λ at wavelength λ ~~finally expresses as follows~~is calculated as shown
270 in Eq. 6:

271

272 $I_\lambda(\psi) = I_{\lambda,0} \times [a_\lambda - b_\lambda \cos(4\psi)]$ (6)

11

273

274　where the intensity $I_{\lambda,0} = \eta_\lambda P_\lambda/(4d^2)$, while coefficients a_λ and b_λ are equal to $a_\lambda = F_{11,\lambda} + F_{22,\lambda}$ and $b_\lambda = 3F_{22,\lambda} - F_{11,\lambda}$.

275　Hence, $F_{22,\lambda}/F_{11,\lambda} = (1 + b_\lambda/a_\lambda)/(3 - b_\lambda/a_\lambda)$ so that the ratio $F_{22,\lambda}/F_{11,\lambda}$ at π−angle can be determined from the ratio

276　b_λ/a_λ . This ratio can be obtained ~~by recording the variations~~ from measurements of $I_\lambda(\psi)$, for different ψ-angles of the QWP,

277　then adjusting these variations with Eq. (6) to get accurate determinations of $I_{\lambda,0}a_\lambda$ and $I_{\lambda,0}b_\lambda$, then b_λ/a_λ. ~~Accurate~~

278　~~e~~Evaluations of the dust lidar *PDR* are then finally retrieved from Eq. (4):

279

280　$PDR_\lambda = (1 - b_\lambda/a_\lambda)/2$ （7）

281

282　Within our methodology, the dust lidar *PDR* is independent of $I_{\lambda,0}$. For that reason, in Section 4, the applied voltage to the UV

283　and VIS-photodetectors is ~~will be~~ adjusted to each dust *SD* and mineralogy to gain in accuracy in the retrieved dust lidar *PDR*

284　by improving the signal-to-noise ratio on I_λ. ~~To fix ideas,~~ For example, ~~we numerically simulated in Figure~~ Fig. 3 provides

285　simulations of ~~the variations of~~ $I_\lambda(\psi)/I_{\lambda,0}$ for the three following dust lidar *PDR* case studies : 33 % dust lidar *PDR* (in full

286　lines, i.e. $F_{22,\lambda}/F_{11,\lambda} = 0.5$), 25 % dust lidar *PDR* (in dashed-lines, i.e. $F_{22,\lambda}/F_{11,\lambda} = 0.6$), 10 % dust lidar *PDR* (in dotted

287　lines, i.e. $F_{22,\lambda}/F_{11,\lambda} = 0.82$). The curve minima, which are equal to $I_{\lambda,m}/I_{\lambda,0} = a_\lambda - b_\lambda = F_{11,\lambda} - F_{22,\lambda}$, are shape-dependent

288　: each curve hence exhibits non-vanishing minima since mineral dust particles are nonspherical. Likewise, the curve maxima

289　are equal to $I_{\lambda,M}/I_{\lambda,0} = a_\lambda + b_\lambda = 2F_{22,\lambda}$ and are size-dependent, though it is also shape dependent. The dust lidar *PDR* is

290　determined from $I_{\lambda,m}$ and $I_{\lambda,M}$ since, following Eq. (7), $PDR_\lambda = I_{\lambda,m}/(I_{\lambda,m} + I_{\lambda,M})$, independently of $I_{\lambda,0}$.
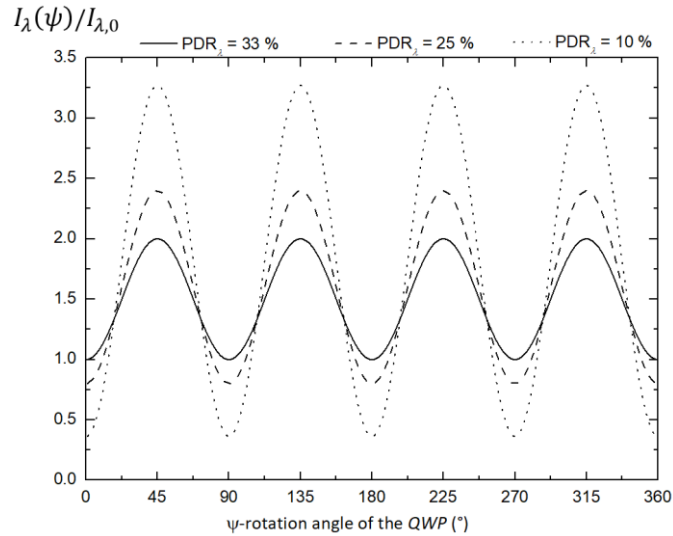
291

292　Figure 3: Numerical simulation of the dust backscattered light intensity $I_\lambda(\psi)/I_{\lambda,0}$ as a function of the orientation ψ of the *QWP* at a given
293　wavelength at the three following case studies: $PDR_\lambda = 33$ % (in full lines, corresponding to $F_{22,\lambda}/F_{11,\lambda} = 0.50$), : $PDR_\lambda = 25$ % (in
294　dashed-lines, $F_{22,\lambda}/F_{11,\lambda} = 0.60$), : $PDR_\lambda = 10$ % (in dotted lines, $F_{22,\lambda}/F_{11,\lambda} = 0.82$).

3.5 Accuracy on the retrieved laboratory mineral dust lidar PDR

Special care has been taken to quantify the uncertainties on the retrieved dust lidar PDR. The systematic errors in the π-polarimeter are that encountered in 2λ-polarization lidar experiments, which we extensively studied (David et al., 2012) and can also be found in polarization lidar reference papers (Freudenthaler, 2016). To summarize, systematic errors arise from:

- *Imperfect definition of the polarization state of the incident radiation.* In the π–polarimeter, the polarization state of the electromagnetic radiation ~~emerging~~ emitted from the laser is precisely set to $[1, 1, 0, 0]^T$ (i.e. with no remaining ellipticity) by using two successive PBC.

- *Polarization cross-talk~~s~~ between the emitter and the detector polarization axes.* Likewise, on the detector side, to account for the imperfections of the retro-reflecting PBC ($R_s > 99.5\,\%$, $T_p > 90\,\%$), a secondary PBC is inserted between the retro-reflecting PBC and the light detector to ensure polarization cross-talk or undesired fraction $R_p T_s$ originating from the p-component of the backscattered radiation ~~to be~~are fully negligible. Hence, the π–polarimeter is sensitive to the s-component of the backscattered radiation only. Also, the emitting PBC being used as retro-reflecting PBC, any possible mismatch between the s-polarization axis of the emitted and detected backscattered radiations cannot occur.

- *Spectral cross-talk~~s~~ between the UV and the VIS-backscattered radiations.* Likewise, wavelength cross-talk is~~s~~ ~~are~~ minimized by using selective interference filters exhibiting a higher than 5 optical density, at 355 nm wavelength in the VIS π–polarimeter and at 532 nm wavelength in the UV π–polarimeter.

- *Multiple scattering can induce further light depolarization.* However, the single-scattering approximation is ~~is rather safe~~ensured~~e~~ in our laboratory backscattering experiment (Mishchenko et al., 2007) where the particles are moving in a thin (2.5 mm) wide beam so that the volume element is optically thin in contrary to atmospheric chambers~~.~~ (1100 cm^{-3} for the coarser SD).

Finally, to account for potential fluctuations in the dust particle number concentration that may cause variations in the dust backscattered light intensity I_λ, a normalization channel has been added to ~~our experiment~~the π-polarimeter by including ~~considering~~ a polarization-insensitive light detector operating at scattering angle $\theta_0 = 165°$. The corresponding scattered light intensity $I_\lambda(\theta_0)$ is quantified ~~can be retrieved from the Mueller matrices successively encountered by the laser pulse~~similarly to Eq. 5 considering a ~~at~~scattering angle of θ_0 : $I_\lambda(\theta_0) = [1, 0, 0, 0]^T [\mathbf{F}_\lambda(\theta_0)][\mathbf{QWP}(\psi)][\mathbf{PBC}][1, 1, 0, 0]^T$, where $[\mathbf{F}_\lambda(\theta_0)]$ is the scattering matrix at angle θ_0~~(. there~~There, the QWP and the PBC only act on the detector side while (St_i) equals $[1, 1, 0, 0]^T$~~.)~~ ~~to~~Hence, ~~get~~ $I_\lambda(\theta_0) = I_{\lambda,0} \times \left[2F_{11,\lambda}(\theta_0) + F_{12,\lambda}(\theta_0) + F_{12,\lambda}(\theta_0)\cos(4\psi)\right]$. Once the variations of $I_\lambda(\theta_0)$ with ψ-angle are recorded, the $\cos(4\psi)$-dependency of $I_\lambda(\theta_0)$ can be removed by applying a numerical low-pass filter on $I_\lambda(\theta_0)$, to get a light intensity proportional to the dust particles number concentration. As a result, in the light backscattering curves presented in Section 4, the plotted quantity is the normalized backscattered light intensity $I_{\lambda,N} = I_\lambda(\pi)/I_\lambda(\theta_0)$, which is

327   insensitive to potential fluctuations in the dust particles number concentration. The scattered light intensities $I_\lambda(\pi)$ and

328   $I_\lambda(\theta_0)$ being correlated, the standard deviation σ_N on $I_{\lambda,N}$ was calculated by considering the covariance $\sigma_{I_\lambda I_\lambda(\theta_0)}$ of I_λ and

329   $I_\lambda(\theta_0)$. This covariance contributes to the uncertainty on $I_{\lambda,N}$ at a rate $-2I_\lambda\sigma_{I_\lambda I_\lambda(\theta_0)}/I_\lambda^3(\theta_0)$. Moreover, to gain in accuracy in

330   the dust lidar PDR retrievals, $I_{\lambda,N}$ was measured for a complete ψ-angle rotation, while averaging the acquired backscattered

331   light intensity over several thousand laser shots per ψ-angle, with resulting mean and standard deviations on $I_{\lambda,N}$ as plotted in

332   ~~Figures~~ Fig. 4 and 5.

4. Results and discussion

334   In this section, using the methodology presented in Section 3, the lidar PDR of Arizona dust, Asian dust, silica and hematite

335   is evaluated and discussed at 355 and 532 nm wavelength for the finer and the coarser SD.

4.1 Laboratory evaluation of the lidar PDR of Arizona and Asian dust

337   Figure 4 displays the variations of $I_{\lambda,N}$ for Arizona (Fig. 4a) and Asian dust (Fig. 4b) as a function of the ψ-rotation angle

338   of the QWP for the finer (left panels) and the coarser SD (right panels) at 355 and 532 nm wavelength. The observed variations

339   are related to a determined size and shape distribution of the dust sample: indeed, as explained in Section 3.4, if the size (resp.

340   the shape) of the dust sample was varying during our acquisitions, the maxima (resp. the minima) of the curves would not

341   remain constant. As a result, the observed variations of $I_{\lambda,N}$ reveal the spectral and polarimetric backscattering characteristics

342   of each considered dust sample. Therefore, the experimental data points could be fitte~~adjuste~~d with Eq. (6) to evaluate

343   $F_{22,\lambda}/F_{11,\lambda}$ then the dust lidar PDR by applying Eq. (7). Table 1 presents the retrieved values of $F_{22,\lambda}/F_{11,\lambda}$ and of dust lidar

344   PDR. The ~~accuracy~~ uncertainty on $F_{22,\lambda}/F_{11,\lambda}$ results from the ~~accuracy~~ measurement errors of the laboratory π-polarimeter

345   and leads to accurate evaluations of the dust lidar PDR. Within experimental error bars, the lidar PDR of Arizona and Asian

346   dust clearly differ, whatever the chosen wavelength. The generally admitted value of around 33 % for the dust lidar PDR

347   (Tesche et al., 2009) is only obtained for Arizona dust: Asian dust exhibits a lower PDR in the range from 24 to 28 % depending

348   on the considered SD and wavelength. This suggests that the dust lidar PDR is primarily governed by the dust mineralogy and

349   hence particles refractive index. The sensitivity of the dust lidar PDR with the considered SD is indeed less pronounced: from

350   the coarser to the finer SD, a reduction in the dust lidar PDR of below 5 % is observed at 532 nm wavelength. At 355 nm

351   wavelength however, the Arizona and Asian dust lidar PDR seem practically insensitive to variations in the considered SD.

(a)

(b)

352

15
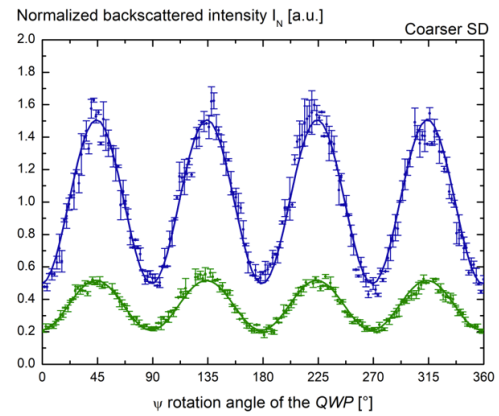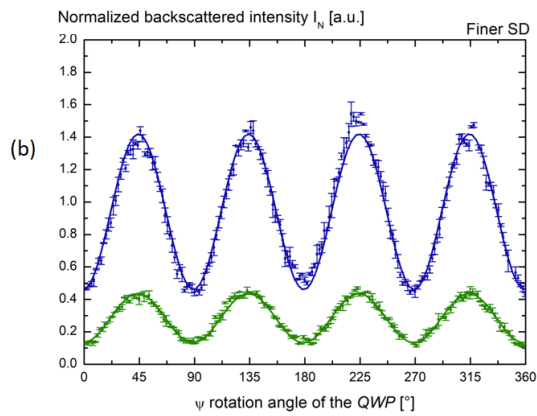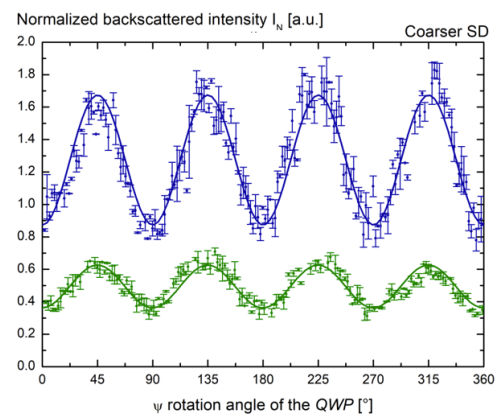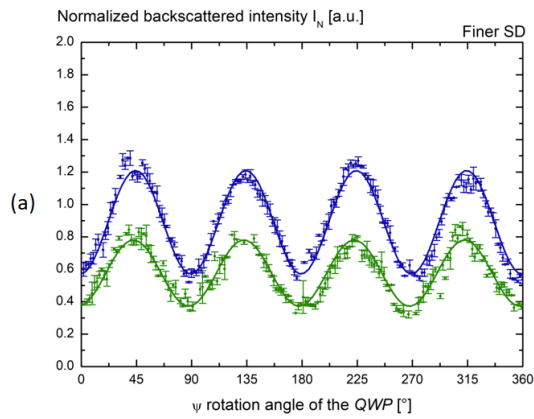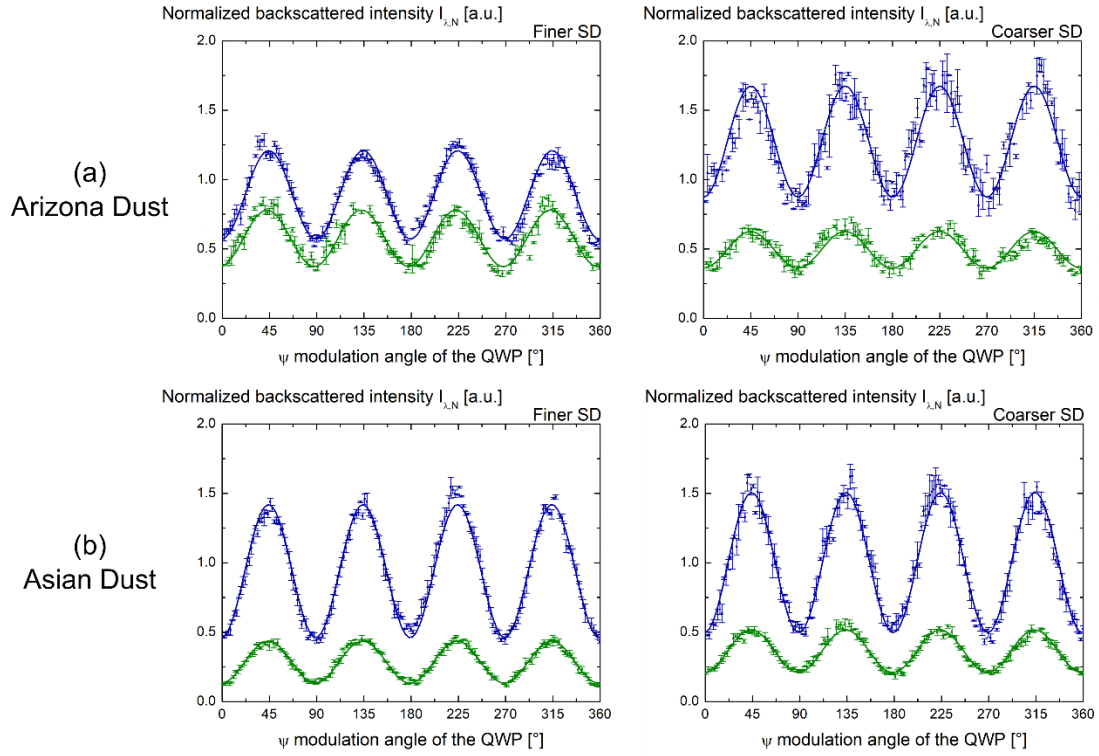
Figure 4: Normalized backscattered light intensity $I_{\lambda,N} = I_\lambda(\pi)/I_\lambda(\theta_0)$ ~~of~~by Arizona (a) and Asian dust (b) for ~~the~~ finer SD (left panels) and ~~the~~ coarser SD (right panels), using the laboratory π-polarimeter at lidar exact backscattering angle ($\theta = \pi$) at 355 (blue) and 532 (green) nm ~~wavelength~~. The experimental data points are ~~adjusted~~ fitted with Eq. ~~(6)~~ to derive ~~evaluate~~ $F_{22,\lambda}/F_{11,\lambda}$ and then the dust lidar PDR is derived using ~~by applying Eq~~Eq. ~~(7)~~. Care should be taken when comparing $I_{\lambda,N}$ for Arizona and Asian dust ~~since~~for the applied voltage to the UV and VIS-photodetectors w~~as~~ere adjusted to increase the signal-to-noise ratio, as explained in Section 3.4. ~~Hence, t~~ The Arizona dust lidar PDR, retrieved from $I_{\lambda,m}/(I_{\lambda,m} + I_{\lambda,M})$, is higher than that of Asian dust.

Tab. 1: Laboratory measurement of the ~~lidar~~ PDR of Arizona and Asian dust at 355 (blue) and 532 nm (green), ~~wavelength~~ for the finer and the coarser SD. The ~~lidar~~ PDR is calculated with ~~retrieved by applying~~ Eq. (7) after the derivation of ~~accurate evaluations of~~ $F_{22,\lambda}/F_{11,\lambda}$ using ~~obtained with~~ the laboratory π-polarimeter ~~(Miffre et al., 2016)~~ presented in Section 3.2. The uncertainty on $F_{22,\lambda}/F_{11,\lambda}$ is deduced from the evaluation of b_λ/a_λ, itself deduced from the least-square fit adjustment of I_λ. The uncertainty on $F_{22,\lambda}/F_{11,\lambda}$ is mostly dominated by statistical uncertainties since our biases are minimized, as explained in Section 3.5.
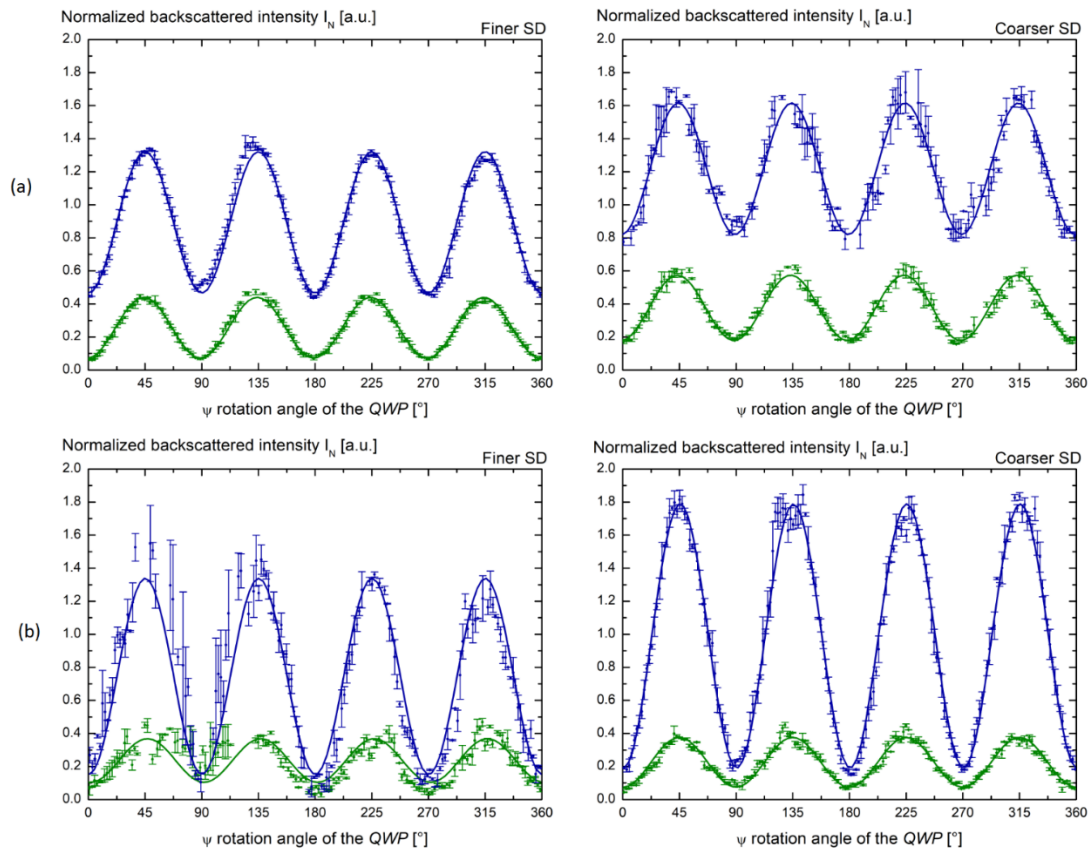
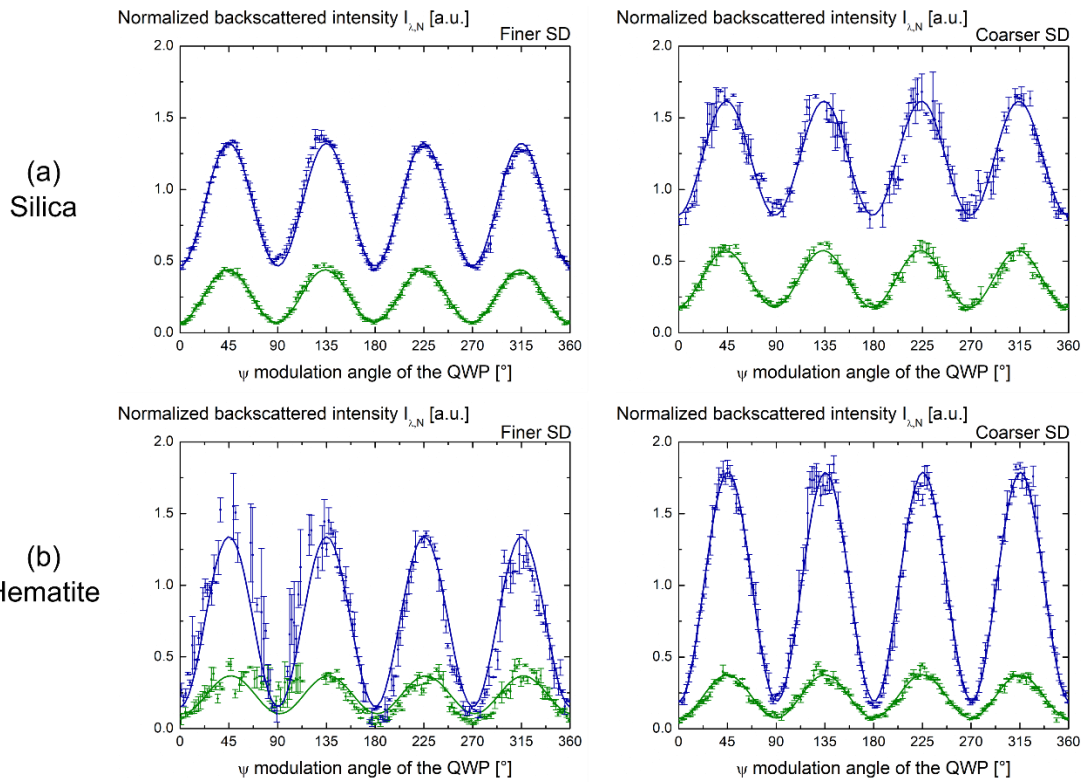| Mineralogy	λ	Finer SD		Coarser SD	
	(nm)	$F_{22,\lambda}/F_{11,\lambda}$	PDR_λ (%)	$F_{22,\lambda}/F_{11,\lambda}$	PDR_λ (%)
Arizona dust	355	0.514 ± 0.007	32.1 ± 0.6	0.489 ± 0.012	34.3 ± 1.0
	532	0.512 ± 0.012	32.3 ± 1.0	0.464 ± 0.012	36.6 ± 1.1
Asian dust	355	0.603 ± 0.009	24.7 ± 0.6	0.603 ± 0.011	24.8 ± 0.8
	532	0.622 ± 0.009	23.3 ± 0.7	0.558 ± 0.011	28.4 ± 0.8

16

4.2 Laboratory evaluation of the lidar *PDR* of silica and hematite

By applying the same methodology, we obtain the ~~lidar~~ *PDR* of silica and hematite ~~were obtained~~, as presented in Fig. 5 and Table 2 ~~which is the analogue of Table 1 for silica and hematite~~. Accordingly, ~~Figure~~ Fig. 5 is the analog of ~~Figure~~ Fig. 4 for silica (Fig. 5a) and hematite (Fig. 5b). As for Arizona and Asian dust samples, the lidar *PDR* of silica and hematite primarily depends on the particles *CRI*, at least at 355 nm wavelength where the silica lidar *PDR* ranges from 23 to 33 % depending on the considered *SD* while the hematite lidar *PDR* reaches 10 % only. The silica lidar *PDR* also strongly depends on ~~the *D* :~~ the particles diameter: from the coarser to the finer SD, the silica dust lidar PDR reduces by 10 % at both wavelengths. The dependence of the hematite dust lidar *PDR* with the *SD* is less pronounced, especially at 355 nm wavelength. The silica and hematite lidar *PDR* also strongly depend on the chosen lidar wavelength, with higher depolarization observed at 355 nm wavelength for silica and at 532 nm wavelength for hematite.

17

Figure 5: Same as ~~Figure~~ Fig. 4 for silica (a-plots) and for hematite _samples_ (b-plots).

Tab. 2: Same as Table 1 for silica and hematite.

Mineralogy	λ	Finer SD		Coarser SD	
	(nm)	$F_{22,\lambda}/F_{11,\lambda}$	PDR_λ (%)	$F_{22,\lambda}/F_{11,\lambda}$	PDR_λ (%)
Silica	355	0.622 ± 0.014	$\mathbf{23.3 \pm 0.9}$	0.506 ± 0.011	$\mathbf{32.8 \pm 1.0}$
	532	0.751 ± 0.016	$\mathbf{14.2 \pm 0.9}$	0.618 ± 0.016	$\mathbf{23.6 \pm 1.1}$
Hematite	355	0.805 ± 0.050	$\mathbf{10.8 \pm 2.5}$	0.823 ± 0.015	$\mathbf{9.7 \pm 0.7}$
	532	0.652 ± 0.055	$\mathbf{21.1 \pm 3.5}$	0.715 ± 0.019	$\mathbf{16.6 \pm 1.1}$

4.3 Discussion

Comparing our laboratory findings with other laboratory experiments is not straightforward, since as explained in the introduction, none operates at 180.0° lidar exact backscattering angle, while the dust lidar PDR differs from near to exact

390 backscattering angles~~,~~, especially when light absorbents are ~~involved~~present (Cholleton et al., 2022). ~~Otherwise~~Moreover, the

391 ~~lidar~~ *PDR* is wavelength-dependent and the size distributions (*SD*) used are different from other studies. ~~Though our samples~~

392 ~~may somewhat differ, (Sakai et al., (2010) retrieved increasing lidar PDR with size at 532 nm wavelength, what we also~~

393 ~~observe.~~ Lidar field experiments provide accurate values of the lidar *PDR* after accurate calibration procedure based on the

394 scattering matrix (Freudenthaler, 2016; Belegante et al., 2018; Miffre et al., 2019). Alt~~Th~~ough in such lidar field experiments,

395 the measured *PDR* is usually ~~nevertheless~~ that of dust ~~particle~~ mixtures (Miffre et al., 2011), the comparison with our

396 laboratory findings remains interesting ~~as a complement~~. In lidar retrievals (see for example (Tesche et al., 2009)), a dust lidar

397 *PDR* of ~~in the range of~~ 30 % is often used.~~considered.~~ The laboratory π-polarimeter verifies this ~~validates that~~ statement by

398 providing the silica ~~lidar~~ *PDR*, which is the main oxide present in mineral dust, equal to (33 ± 1) % for the coarser *SD* at 355

399 nm. In comparison, within our experimental error bars, the hematite lidar *PDR*, equal to (10 ± 1) %, is clearly lower. The real

400 part n and the imaginary part κ of the hematite *CRI*, which are large compared with that of other chemical oxides present in

401 mineral dust (see Section 2.1), can be responsible for the observed difference in the silica and hematite lidar *PDR*. Indeed, n

402 and part κ modify the backscattering matrix elements, so does the corresponding dust lidar *PDR*. To highlight the role of κ on

403 the hematite lidar *PDR*, the lidar *PDR* of rutile was measured with our π-polarimeter. Indeed, the real part of the rutile *CRI* is

404 as large as that of hematite but its imaginary part is negligible compared with that of hematite. As a result, the rutile lidar *PDR*

405 substantially differed from that of hematite, showing the key role played by light absorption in the measured hematite lidar

406 *PDR*. In turn, Arizona dust exhibits a higher *PDR* than Asian dust, due to the higher proportion in hematite in the latter. Hence

407 and as a conclusion, our laboratory findings show that, when the light absorbent hematite is present, it mainly governs the dust

408 lidar *PDR*, which hence primarily depends on the particles mineralogy, with less pronounced variations with the particles size

409 and wavelength. This finding is in line with (Kahnert, 2015; Kahnert et al., 2020) numerical findings, who highlighted that the

410 dust *PDR* is strongly modulated by the particles inhomogeneity, especially in the lidar backward scattering direction and in

411 the presence of hematite. We here quantify this effect with a laboratory experiment that accounts for the real shape of mineral

412 dust. The shape dependence of the hematite PDR is weak due to its large imaginary part of complex refractive index: following

413 (Wiscombe and Mugnai~~,~~ (1986) or (Mishchenko et al.~~,~~ (1997), the effect of particle shape becomes weaker with increasing

414 imaginary part of the refractive index, a conclusion also drawn by (Meland et al.~~,~~ (2011). In contrast, w~~W~~hen the proportion

415 of hematite becomes negligible, as is the case for silica and Arizona dust, our laboratory findings show that the dust lidar *PDR*

416 then increases with increasing the particles size, though the shape dependence may then also play a role. Also, it would be

417 interesting to investigate giant dust particles (Ryder et al., 2019). Likewise, in the literature (Sakai et al., 2010; Hofer et al.,

418 2020; Järvinen et al., 2016; Mamouri and Ansmann, 2017), the dust lidar *PDR* is usually found to increase with the particles

419 size from the fine to the coarse mode of the *SD*. The $(355, 532)$ nm wavelength dependence of the dust lidar *PDR* then becomes

420 key for discussing on the involved particle sizes, thus underlying the importance of dual-wavelength (or more) polarization

421 lidar instruments. We here establish this result in laboratory at $180.0°$ and $(355, 532)$ nm wavelength, and moreover, show that

422   this consideration holds only when hematite, which is a strong light absorbent, is not involved : the hematite lidar PDR is

423   indeed higher in the finer mode of the SD.

424

425   To go further and discuss on the role of light absorption in the retrieved dust lidar PDR, we here propose a basic partitioning

426   model in which the dust particles mixture $(d) = \{Abs, \overline{Abs}\}$ is ~~resumed to~~comprised of two components: an absorbing

427   component (Abs), mainly corresponding to hematite particles, and a non-absorbing component $(\overline{Abs})$, mainly corresponding

428   to silica-particles. For simplicity, we here resume the absorbing (resp. non-absorbing) component to hematite (resp. silica)-

429   particles with respective abbreviations (Hmt) and (Sil). We focus on the 355 nm wavelength at which hematite is an efficient

430   light absorber and on the coarser SD as the dependence of the dust lidar PDR with size is less pronounced than with the

431   particles mineralogy. In Appendix A is detailed the derivation of the lidar PDR of such a dust-particles mixture $(d) =$

432     $\{Hmt, Sil\}$ (hereafter noted δ_d, as in lidar applications). This Appendix is an extension of our previous works (Miffre et al.,

433   2011; David et al., 2013, 2014; Mehri et al., 2018) ~~to~~ for the case study where ~~where~~ both components $\{Hmt, Sil\}$ are

434   nonspherical. The lidar PDR of such a dust-particles mixture relates to that of its pure components (hereafter noted

435   δ_{Sil} and δ_{Hmt}) as follows:

436

437     $$\delta_d = \frac{-e + (c + e)X_{\text{Hmt}}}{f - (d + f)X_{\text{Hmt}}} \tag{8}$$

438

439   where the expressions of the c, d, e and f-coefficients are ~~given~~ provided in Appendix A and ~~in~~only dependently~~d~~ on the

440   depolarization ratios δ_{Sil} and δ_{Hmt} of silica and iron oxides. X_{Hmt} is the fraction of Hmt to dust particles backscattering.

441   Following Eq. (8) and Appendix A, ~~Figure~~ Fig. 6 displays the variation of δ_d as a function of X_{Hmt} when considering $\delta_{Sil} =$

442   33 % and $\delta_{Hmt} = 10$ %, as obtained in our laboratory findings at 355 nm wavelength with the coarser SD. As shown in ~~Figure~~

443   Fig. 6, the dust lidar PDR lies in between δ_{Sil} and δ_{Hmt} and equals δ_{Sil} (resp. δ_{Hmt}) only when $X_{Hmt} = 0$ (resp. 1), depending

444   on the fraction X_{Hmt} of light corresponding to the absorbent of~~in~~ the dust particle mixture. Hence, Arizona dust, which contains

445   a lower fraction of hematite, exhibits a higher lidar PDR compared with Asian dust, at least at 355 nm wavelength where

446   hematite is strongly absorbing. Though rather simple, our model interestingly highlights the key role played by light absorption

447   in the retrieved Asian dust lidar PDR. To go further and provide ~~become~~ a quantitative analysis, this simple model should be

448   refined, by considering also the other chemical oxides present in mineral dust, ~~as well as other SD and~~ other lidar wavelengths,

449   as well as other SD and the effect of shape. To handle such a complex issue, more laboratory experiments are required on other

450   chemical oxides, ideally also at 1064 nm wavelength. This work is however beyond the scope of this paper. Still as is, our

451   model provides an interpretation of the laboratory-observed differences in the dust lidar PDR when the light absorbent hematite

452   is involved. In the most general case, the dust lidar PDR hence appears as a complex function of the particles mineralogy,

453     $SD,$ ~~and~~ wavelength and shape. Comparison with lidar field experiments, involving particle mixtures, with a more complex

454 distribution of sizes and refractive indices, is then not straightforward, as underscored by comparison with (Hu et al., (2020)

455 who reported 0.28 - 0.32 ± 0.07 at 355 nm wavelength. Though this triple complex -dependence is difficult to disentangle, our

456 laboratory findings show that the dust lidar *PDR* is primarily affected by the particles mineralogy, at least when hematite is

457 involved.
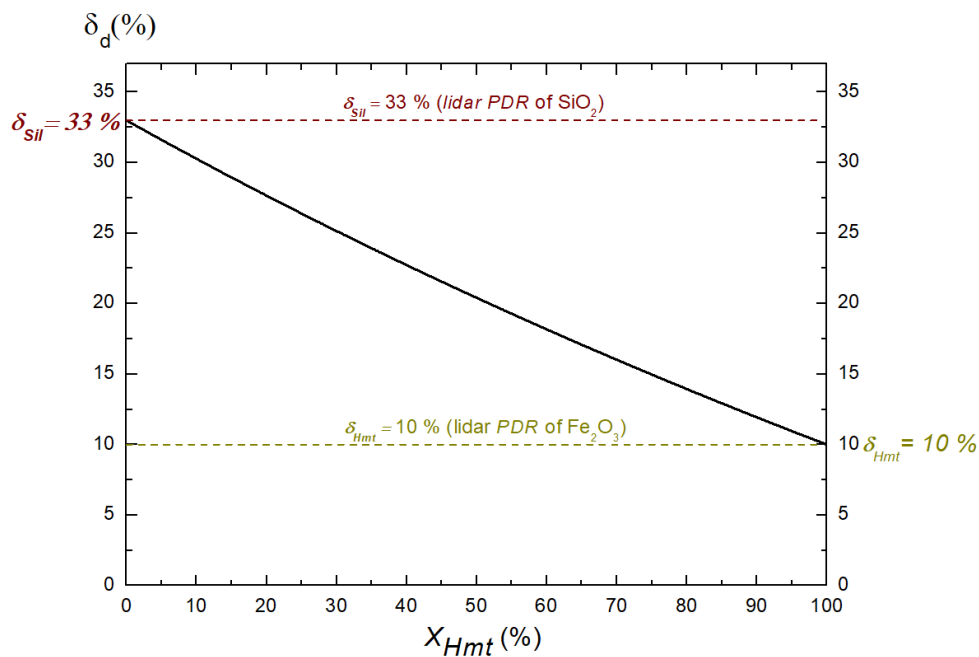
458
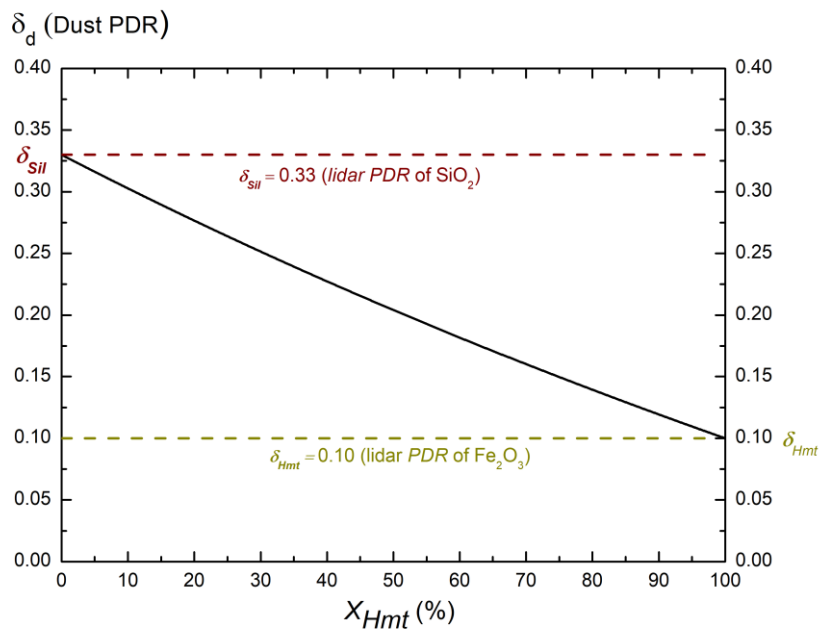
459

460 Figure 6: Numerical simulation of the 355 nm Lidar PDR of a two-component particles mixture $(d) = \{Hmt, Sil\}$, composed ~~of a light~~of
461 hematite (Hmt) and silica (Sil) oxides as a function of the $X_{Hmt} = \beta_{Hmt}/\beta_d$ fraction of Hmt to d-particles backscattering, following Eq.
462 (8) and Appendix A, by accounting for our laboratory experimental findings for δ_{Sil} = 33 % and δ_{Hmt} = 10 % (see Table 2 at 355 nm
463 wavelength with coarser SD).

5 Summary and ~~Conclusion~~conclusion

465 In this paper, the dependence of the lidar particles depolarization ratio (PDR) of pure mineral dust with complex refractive
466 index (CRI) and size is for the first time investigated through a laboratory π-polarimeter operating at 180.0° lidar
467 backscattering angle and (355, 532) nm wavelengths for lidar purposes. The goal of this work is to improve the knowledge on
468 the dust lidar PDR, which is an important input parameter involved in lidar partitioning algorithms, which are widely applied
469 to reveal the contribution of mineral dust in particles external mixtures (Tesche et al., 2009; Mehri et al., 2018). While mineral
470 dust exhibits a complex and highly irregular shape, which is difficult to model mathematically and numerically, our laboratory
471 approach allows accounting for the real shape of mineral dust. Our laboratory π-polarimeter is likewise a good complement to
472 lidar field experiments, which provide accurate retrievals of the lidar PDR of particles mixtures involving mineral dust.
473 Another advantage of our laboratory π-polarimeter lies in its ability to provide accurate retrievals of the lidar PDR of pure
474 mineral dust samples, differing in CRI and size. The π-polarimeter indeed operates at 180.0° lidar backscattering angle and at
475 (355, 532) nm lidar wavelengths: no assumption is made to retrieve the dust lidar PDR. This is a key novelty of our study.
476 Indeed, the variation of the dust lidar PDR with scattering angle and wavelength cannot be ~~quantified~~ analytically calculated
477 (Bohren and Huffman, 1983; Mishchenko et al., 2002) for complex-shaped particles such as mineral dust. Hence, our π-
478 polarimeter improves the knowledge on the dust PDR, ~~which are given~~ provided in the literature at non 180.0° backscattering
479 angle and / or at wavelengths differing from (355, 532 nm). Our work provides sixteen accurate dust lidar PDR-values,
480 corresponding to four different complex refractive indices, studied at two size distributions (fine, coarse) and at (355, 532) nm
481 wavelengths (see Section 4). The precision on the retrieved dust ~~lidar~~ PDR ~~originates from the scattering matrix formalism,~~
482 ~~on which~~ from the laboratory π-polarimeter ~~is~~relies, as detailed in Section 3. To investigate the dependence of the dust lidar
483 PDR with CRI, hematite, the main light absorbent present in mineral dust, was considered in addition to silica oxide, the main
484 chemical oxide present in mineral dust, which is practically nonabsorbent. At 355 nm, our laboratory π-polarimeter provides
485 ~~proves that~~ values of the ~~lidar~~ PDR of coarser silica ~~of is equal to~~ (33 ± 1) % while that of coarser hematite is only (10 ± 1)
486 %. In Section 4, this ~~huge~~ large difference is explained by accounting for the high imaginary part of the hematite CRI. In turn,
487 Arizona dust exhibits a higher depolarization ratio than Asian dust, due to the higher proportion in hematite in the latter. As a
488 result, when the strong light absorbent hematite is involved, the dust lidar PDR is primarily governed by the particles
489 mineralogy and the variations of the dust lidar PDR with size are less pronounced. The dependence of the PLDR on the
490 particles shape is not pronounced in our experiment where hematite, which exhibits a large imaginary part of complex
491 refractive index, plays a key role (.(Wiscombe and Mugnai, (1986). (Mishchenko et al., (1997). (Meland et al., (2011).
492 When hematite is less or not involved, the dust lidar PDR increases with increasing sizes and the (355, 532) nm wavelength

493 dependence of the dust lidar *PDR* then becomes key for discussing on the involved particle sizes, thus underscoring the

494 importance of dual wavelengths (or more) polarization lidar instruments. To further disentangle the complex dependence of

495 the dust lidar *PDR* with complex refractive index and size, our methodology should be extended to other chemical oxides,

496 other natural mineral dust samples, other *SD* and other wavelengths, as well as other shape distributions. Giant dust particles,

497 whose importance has been highlighted by (Ryder et al., (2019), would likewise be interesting to study specifically. This is

498 however far beyond the scope of this paper : we here focused on (355, 532) nm wavelengths, since mineral dust slightly absorb

499 light in the near infra-red (Di Biagio et al., 2019). Still, the above laboratory findings underscore the importance of accounting

500 for the wavelength dependence of the dust lidar *PDR*, whatever the hematite proportion. The spectral dependence of the dust

501 lidar *PDR* is indeed instructive (Burton et al., 2016; Haarig et al., 2022; Miffre et al., 2020). Numerical oOutlooks of this work

502 are obviously also interesting, as underscored by recent papers (Kahnert et al., 2020; Luo et al., 2022), discussing on the ability

503 of the spheroidal model to mimic light scattering by complex-shaped mineral dust.

504 **Appendix A**

505 The goal of this Appendix is to establish the expression of the lidar *PDR* of a two-component particle mixture $(p) =$

506 $\{ns_1, ns_2\}$ composed of two non-spherical components ns_1 and ns_2. As in lidar applications, the lidar *PDR* of p, ns_1 and ns_2-

507 particles are respectively noted δ_p, δ_{ns_1} and δ_{ns_2}. The starting point is given by the set of four equations:

508

509 $\beta_{p,//} = \beta_{ns_1,//} + \beta_{ns_2,//}$ (A-1-a)

510 $\beta_{p,\perp} = \beta_{ns_1,\perp} + \beta_{ns_2,\perp}$ (A-1-b)

511 $\delta_{ns_1} = \beta_{ns_1,\perp}/\beta_{ns_1,//}$ (A-1-c)

512 $\delta_{ns_2} = \beta_{ns_2,\perp}/\beta_{ns_2,//}$ (A-1-d)

513

514 where $\beta_{p,//}$ and $\beta_{p,\perp}$ are the lidar particles backscattering coefficients, evaluated from a polarization lidar experiment carried

515 out at wavelength λ (here omitted to ease the reading). The backscattering coefficient β_{ns_1} of ns_1-particles is then retrieved by

516 noting that $\beta_{ns_1} = \beta_{ns_1,//} + \beta_{ns_1,\perp} = \beta_{ns1,\perp}(1 + 1/\delta_{ns_1})$ (Miffre et al., 2011; David et al., 2013). Moreover, $\beta_{ns_1,\perp}$ can be

517 expressed as a fonction of $\beta_{p,//}$ and $\beta_{p,\perp}$ since $\beta_{ns_1,\perp} = \beta_{p,\perp} - \beta_{ns_2,\perp} = \beta_{p,\perp} - \delta_{ns_2}\beta_{ns_2,//} = \beta_{p,\perp} - \delta_{ns_2}(\beta_{p,//} - \beta_{ns_1,\perp}/\delta_{ns_1})$

518 using Eqs. (A-1). Hence, $\beta_{ns_1,\perp} = (\beta_{p,\perp} - \delta_{ns_2}\beta_{p,//})/(1 - \delta_{ns_2}/\delta_{ns_1})$. By applying the same methodology to ns_2- particles,

519 we finally get:

520

521 $\begin{pmatrix} \beta_{ns_1} \\ \beta_{ns_2} \end{pmatrix} = \begin{bmatrix} c & d \\ e & f \end{bmatrix} \begin{pmatrix} \beta_{p,//} \\ \beta_{p,\perp} \end{pmatrix}$ (A-2)

522

where the c, d, e and f-coefficients only depend on the depolarization ratios δ_{ns_1} and δ_{ns_2} :

$c = -\delta_{ns_2}(1 + 1/\delta_{ns_1})/(1 - \delta_{ns_2}/\delta_{ns_1})$ (A-3-a)

$d = (1 + 1/\delta_{ns_1})/(1 - \delta_{ns_2}/\delta_{ns_1})$ (A-3-b)

$e = -\delta_{ns_1}(1 + 1/\delta_{ns_2})/(1 - \delta_{ns_1}/\delta_{ns_2})$ (A-3-c)

$f = (1 + 1/\delta_{ns_2})/(1 - \delta_{ns_1}/\delta_{ns_2})$ (A-3-d)

The 2 x 2 matrix introduced in Eq. (A-2) can be inverted to get the expression of $\beta_{p,//}$ and $\beta_{p,\perp}$ and hence $\delta_p = \beta_{p,\perp}/\beta_{p,//}$. By introducing $X_{ns2} = \beta_{ns2}/(\beta_{ns1} + \beta_{ns2})$ the fraction of ns_2 to p-particles backscattering, we finally get the relationship between δ_p and δ_{ns1} and δ_{ns2} :

$$\delta_p = \frac{-e + (c + e)X_{ns2}}{f - (d + f)X_{ns2}} \qquad (A-4)$$

In the specific case where ns_2-particles are spherical (i.e. $\delta_{ns_2} = 0$), the expressions of the c, d, e and f-coefficients simplify and the relationship between δ_p and $X_{ns2} = X_{ns}$ becomes identical to that we already published in (Miffre et al., 2011; David et al., 2013). This new material is hence as an extension of our previous works (Miffre et al., 2011; David et al., 2013, 2014; Mehri et al., 2018) to the case study where both components of the particles mixture $(p) = \{ns_1, ns_2\}$ are nonspherical.

Author contribution

Alain Miffre: Conceptualization, Formal analysis, Investigation, Methodology, Supervision, Writing - original draft, Writing - review & editing **Danaël Cholleton**: Formal analysis, Investigation, Software, Visualization, Writing - review & editing. **Clément Noël**: Software, Writing - review & editing **Patrick Rairoux**: Project administration, Supervision, Writing - review & editing.

Competing interests

The authors declare that they have no conflict of interest.

Acknowledgements

References

Belegante, L., Bravo-Aranda, J. A., Freudenthaler, V., Nicolae, D., Nemuc, A., Ene, D., Alados-Arboledas, L., Amodeo, A., Pappalardo, G., D'Amico, G., Amato, F., Engelmann, R., Baars, H., Wandinger, U., Papayannis, A., Kokkalis, P., and Pereira, S. N.: Experimental techniques for the calibration of lidar depolarization channels in EARLINET, Atmospheric Meas. Tech., 11, 1119–1141, https://doi.org/10.5194/amt-11-1119-2018, 2018.

Bohren, C. F. and Huffman, D. R.: Absorption and scattering of light by small particles, Wiley-VCH, Weinheim, 530 pp., 1983.

Bristow, C. S., Hudson-Edwards, K. A., and Chappell, A.: Fertilizing the Amazon and equatorial Atlantic with West African dust: AFRICAN FERTILIZER FOR AMAZON AND ATLANTIC, Geophys. Res. Lett., 37, n/a-n/a, https://doi.org/10.1029/2010GL043486, 2010.

Bullard, J. E. and White, K.: Quantifying iron oxide coatings on dune sands using spectrometric measurements: An example from the Simpson-Strzelecki Desert, Australia, J. Geophys. Res. Solid Earth, 107, ECV 5-1-ECV 5-11, https://doi.org/10.1029/2001JB000454, 2002.

Burton, S. P., Ferrare, R. A., Hostetler, C. A., Hair, J. W., Rogers, R. R., Obland, M. D., Butler, C. F., Cook, A. L., Harper, D. B., and Froyd, K. D.: Aerosol classification using airborne High Spectral Resolution Lidar measurements – methodology and examples, Atmospheric Meas. Tech., 5, 73–98, https://doi.org/10.5194/amt-5-73-2012, 2012.

Burton, S. P., Chemyakin, E., Liu, X., Knobelspiesse, K., Stamnes, S., Sawamura, P., Moore, R. H., Hostetler, C. A., and Ferrare, R. A.: Information content and sensitivity of the $3 \beta + 2 \alpha$ lidar measurement system for aerosol microphysical retrievals, Atmospheric Meas. Tech., 9, 5555–5574, https://doi.org/10.5194/amt-9-5555-2016, 2016.

Caponi, L., Formenti, P., Massabó, D., Di Biagio, C., Cazaunau, M., Pangui, E., Chevaillier, S., Landrot, G., Andreae, M. O., Kandler, K., Piketh, S., Saeed, T., Seibert, D., Williams, E., Balkanski, Y., Prati, P., and Doussin, J.-F.: Spectral- and size-resolved mass absorption efficiency of mineral dust aerosols in the shortwave spectrum: a simulation chamber study, Atmospheric Chem. Phys., 17, 7175–7191, https://doi.org/10.5194/acp-17-7175-2017, 2017.

Cholleton, D., Rairoux, P., and Miffre, A.: Laboratory Evaluation of the (355, 532) nm Particle Depolarization Ratio of Pure Pollen at 180.0° Lidar Backscattering Angle, Remote Sens., 14, 3767, https://doi.org/10.3390/rs14153767, 2022.

David, G., Miffre, A., Thomas, B., and Rairoux, P.: Sensitive and accurate dual-wavelength UV-VIS polarization detector for optical remote sensing of tropospheric aerosols, Appl. Phys. B, 108, 197–216, https://doi.org/10.1007/s00340-012-5066-x, 2012.

David, G., Thomas, B., Nousiainen, T., Miffre, A., and Rairoux, P.: Retrieving simulated volcanic, desert dust and sea-salt particle properties from two/three-component particle mixtures using UV-VIS polarization lidar and T matrix, Atmospheric Chem. Phys., 13, 6757–6776, https://doi.org/10.5194/acp-13-6757-2013, 2013.

David, G., Thomas, B., Dupart, Y., D'Anna, B., George, C., Miffre, A., and Rairoux, P.: UV polarization lidar for remote sensing new particles formation in the atmosphere, Opt. Express, 22, A1009, https://doi.org/10.1364/OE.22.0A1009, 2014.

Di Biagio, C., Formenti, P., Balkanski, Y., Caponi, L., Cazaunau, M., Pangui, E., Journet, E., Nowak, S., Andreae, M. O., Kandler, K., Saeed, T., Piketh, S., Seibert, D., Williams, E., and Doussin, J.-F.: Complex refractive indices and single-scattering albedo of global dust aerosols in the shortwave spectrum and relationship to size and iron content, Atmospheric Chem. Phys., 19, 15503–15531, https://doi.org/10.5194/acp-19-15503-2019, 2019.

587 Dupart, Y., King, S. M., Nekat, B., Nowak, A., Wiedensohler, A., Herrmann, H., David, G., Thomas, B., Miffre, A., Rairoux,
588 P., D'Anna, B., and George, C.: Mineral dust photochemistry induces nucleation events in the presence of SO2, Proc. Natl.
589 Acad. Sci., 109, 20842–20847, https://doi.org/10.1073/pnas.1212297109, 2012.

590 Formenti, P., Caquineau, S., Chevaillier, S., Klaver, A., Desboeufs, K., Rajot, J. L., Belin, S., and Briois, V.: Dominance of
591 goethite over hematite in iron oxides of mineral dust from Western Africa: Quantitative partitioning by X-ray absorption
592 spectroscopy, J. Geophys. Res. Atmospheres, 119, 12,740-12,754, https://doi.org/10.1002/2014JD021668, 2014.

593 Francis, D., Nelli, N., Fonseca, R., Weston, M., Flamant, C., and Cherif, C.: The dust load and radiative impact associated
594 with the June 2020 historical Saharan dust storm, Atmos. Environ., 268, 118808,
595 https://doi.org/10.1016/j.atmosenv.2021.118808, 2022.

596 Freudenthaler, V.: About the effects of polarising optics on lidar signals and the Δ90 calibration, Atmospheric Meas.
597 Tech., 9, 4181–4255, https://doi.org/10.5194/amt-9-4181-2016, 2016.

598 Freudenthaler, V., Esselborn, M., Wiegner, M., Heese, B., Tesche, M., Ansmann, A., MüLLER, D., Althausen, D., Wirth, M.,
599 Fix, A., Ehret, G., Knippertz, P., Toledano, C., Gasteiger, J., Garhammer, M., and Seefeldner, M.: Depolarization ratio profiling
600 at several wavelengths in pure Saharan dust during SAMUM 2006, Tellus B Chem. Phys. Meteorol., 61, 165–179,
601 https://doi.org/10.1111/j.1600-0889.2008.00396.x, 2009.

602 Gasteiger, J., Wiegner, M., GROß, S., Freudenthaler, V., Toledano, C., Tesche, M., and Kandler, K.: Modelling lidar-relevant
603 optical properties of complex mineral dust aerosols, Tellus Ser. B Chem. Phys. Meteorol., 63, 725–741,
604 https://doi.org/10.1111/j.1600-0889.2011.00559.x, 2011.

605 Gautam, P., Maughan, J. B., Ilavsky, J., and Sorensen, C. M.: Light scattering study of highly absorptive, non-fractal, hematite
606 aggregates, J. Quant. Spectrosc. Radiat. Transf., 246, 106919, https://doi.org/10.1016/j.jqsrt.2020.106919, 2020.

607 Glen, A. and Brooks, S. D.: A new method for measuring optical scattering properties of atmospherically relevant dusts using
608 the Cloud and Aerosol Spectrometer with Polarization (CASPOL), Atmospheric Chem. Phys., 13, 1345–1356,
609 https://doi.org/10.5194/acp-13-1345-2013, 2013.

610 Go, S., Lyapustin, A., Schuster, G. L., Choi, M., Ginoux, P., Chin, M., Kalashnikova, O., Dubovik, O., Kim, J., da Silva, A.,
611 Holben, B., and Reid, J. S.: Inferring iron-oxide species content in atmospheric mineral dust from DSCOVR EPIC
612 observations, Atmospheric Chem. Phys., 22, 1395–1423, https://doi.org/10.5194/acp-22-1395-2022, 2022.

613 Gómez Martín, J. C., Guirado, D., Frattin, E., Bermudez-Edo, M., Cariñanos Gonzalez, P., Olmo Reyes, F. J., Nousiainen, T.,
614 Gutiérrez, P. J., Moreno, F., and Muñoz, O.: On the application of scattering matrix measurements to detection and
615 identification of major types of airborne aerosol particles: Volcanic ash, desert dust and pollen, J. Quant. Spectrosc. Radiat.
616 Transf., 271, 107761, https://doi.org/10.1016/j.jqsrt.2021.107761, 2021.

617 Haarig, M., Ansmann, A., Engelmann, R., Baars, H., Toledano, C., Torres, B., Althausen, D., Radenz, M., and Wandinger, U.:
618 First triple-wavelength lidar observations of depolarization and extinction-to-backscatter ratios of Saharan dust, Atmospheric
619 Chem. Phys., 22, 355–369, https://doi.org/10.5194/acp-22-355-2022, 2022.

620 Hofer, J., Ansmann, A., Althausen, D., Engelmann, R., Baars, H., Fomba, K. W., Wandinger, U., Abdullaev, S. F., and
621 Makhmudov, A. N.: Optical properties of Central Asian aerosol relevant for spaceborne lidar applications and aerosol typing
622 at 355 and 532 nm, Atmospheric Chem. Phys., 20, 9265–9280, https://doi.org/10.5194/acp-20-9265-2020, 2020.

Hu, Q., Wang, H., Goloub, P., Li, Z., Veselovskii, I., Podvin, T., Li, K., and Korenskiy, M.: The characterization of Taklamakan dust properties using a multiwavelength Raman polarization lidar in Kashi, China, Atmospheric Chem. Phys., 20, 13817–13834, https://doi.org/10.5194/acp-20-13817-2020, 2020.

Huang, Y., Kok, J. F., Saito, M., and Muñoz, O.: Single-scattering properties of ellipsoidal dust aerosols constrained by measured dust shape distributions, Atmospheric Chem. Phys. Discuss., 1–23, https://doi.org/10.5194/acp-2022-633, 2022.

van de Hulst, H. C.: Light Scattering by Small Particles, Courier Corporation, 500 pp., 1957.

Iwai, T.: Polarization Analysis of Light Scattered by Pollen Grains of *Cryptomeria japonica*, Jpn. J. Appl. Phys., 52, 062404, https://doi.org/10.7567/JJAP.52.062404, 2013.

Järvinen, E., Kemppinen, O., Nousiainen, T., Kociok, T., Möhler, O., Leisner, T., and Schnaiter, M.: Laboratory investigations of mineral dust near-backscattering depolarization ratios, J. Quant. Spectrosc. Radiat. Transf., 178, 192–208, https://doi.org/10.1016/j.jqsrt.2016.02.003, 2016.

Kahnert, M.: Modelling radiometric properties of inhomogeneous mineral dust particles: Applicability and limitations of effective medium theories, J. Quant. Spectrosc. Radiat. Transf., 152, 16–27, https://doi.org/10.1016/j.jqsrt.2014.10.025, 2015.

Kahnert, M., Kanngießer, F., Järvinen, E., and Schnaiter, M.: Aerosol-optics model for the backscatter depolarisation ratio of mineral dust particles, J. Quant. Spectrosc. Radiat. Transf., 254, 107177, 2020.

Kandler, K., Lieke, K., Benker, N., Emmel, C., Küpper, M., Müller-Ebert, D., Ebert, M., Scheuvens, D., Schladitz, A., Schütz, L., and Weinbruch, S.: Electron microscopy of particles collected at Praia, Cape Verde, during the Saharan Mineral Dust Experiment: particle chemistry, shape, mixing state and complex refractive index, Tellus Ser. B Chem. Phys. Meteorol., 63, 475–496, https://doi.org/10.1111/j.1600-0889.2011.00550.x, 2011.

Kosmopoulos, P. G., Kazadzis, S., Taylor, M., Athanasopoulou, E., Speyer, O., Raptis, P. I., Marinou, E., Proestakis, E., Solomos, S., Gerasopoulos, E., Amiridis, V., Bais, A., and Kontoes, C.: Dust impact on surface solar irradiance assessed with model simulations, satellite observations and ground-based measurements, Atmospheric Meas. Tech., 10, 2435–2453, https://doi.org/10.5194/amt-10-2435-2017, 2017.

Lamb, K. D., Matsui, H., Katich, J. M., Perring, A. E., Spackman, J. R., Weinzierl, B., Dollner, M., and Schwarz, J. P.: Global-scale constraints on light-absorbing anthropogenic iron oxide aerosols, Npj Clim. Atmospheric Sci., 4, 1–12, 2021.

Lindqvist, H., Jokinen, O., Kandler, K., Scheuvens, D., and Nousiainen, T.: Single scattering by realistic, inhomogeneous mineral dust particles with stereogrammetric shapes, Atmospheric Chem. Phys., 14, 143–157, https://doi.org/10.5194/acp-14-143-2014, 2014.

Liu, J., Zhang, Q., Huo, Y., Wang, J., and Zhang, Y.: An experimental study on light scattering matrices for Chinese loess dust with different particle size distributions, Atmospheric Meas. Tech., 13, 4097–4109, https://doi.org/10.5194/amt-13-4097-2020, 2020.

Longtin, D. R., Shettle, E. P., Hummel, J. R., and Pryce, J. D.: A wind dependent desert aerosol model: Radiative properties, OPTIMETRICS INC BURLINGTON MA, 1988.

Luo, J., Li, Z., Fan, C., Xu, H., Zhang, Y., Hou, W., Qie, L., Gu, H., Zhu, M., Li, Y., and Li, K.: The polarimetric characteristics of dust with irregular shapes: evaluation of the spheroid model for single particles, Atmospheric Meas. Tech., 15, 2767–2789, https://doi.org/10.5194/amt-15-2767-2022, 2022.

659 Mamouri, R.-E. and Ansmann, A.: Potential of polarization/Raman lidar to separate fine dust, coarse dust, maritime, and
660 anthropogenic aerosol profiles, Atmospheric Meas. Tech., 10, 3403–3427, https://doi.org/10.5194/amt-10-3403-2017, 2017.

661 Mehri, T., Kemppinen, O., David, G., Lindqvist, H., Tyynelä, J., Nousiainen, T., Rairoux, P., and Miffre, A.: Investigating the
662 size, shape and surface roughness dependence of polarization lidars with light-scattering computations on real mineral dust
663 particles: Application to dust particles' external mixtures and dust mass concentration retrievals, Atmospheric Res., 203, 44–
664 61, https://doi.org/10.1016/j.atmosres.2017.11.027, 2018.

665 Meland, B., Kleiber, P. D., Grassian, V. H., and Young, M. A.: Visible light scattering study at 470, 550, and 660nm of
666 components of mineral dust aerosol: Hematite and goethite, J. Quant. Spectrosc. Radiat. Transf., 112, 1108–1118,
667 https://doi.org/10.1016/j.jqsrt.2010.12.002, 2011.

668 Miffre, A., David, G., Thomas, B., and Rairoux, P.: Atmospheric non-spherical particles optical properties from UV-
669 polarization lidar and scattering matrix, Geophys. Res. Lett., 38, L16804, https://doi.org/10.1029/2011GL048310, 2011.

670 Miffre, A., Mehri, T., Francis, M., and Rairoux, P.: UV–VIS depolarization from Arizona Test Dust particles at exact
671 backscattering angle, J. Quant. Spectrosc. Radiat. Transf., 169, 79–90, https://doi.org/10.1016/j.jqsrt.2015.09.016, 2016.

672 Miffre, A., Cholleton, D., Mehri, T., and Rairoux, P.: Remote Sensing Observation of New Particle Formation Events with a
673 (UV, VIS) Polarization Lidar, Remote Sens., 11, 1761, https://doi.org/10.3390/rs11151761, 2019.

674 Miffre, A., Cholleton, D., and Rairoux, P.: On the use of light polarization to investigate the size, shape, and refractive index
675 dependence of backscattering Ångström exponents, Opt. Lett., 45, 1084–1087, https://doi.org/10.1364/OL.385107, 2020.

676 Mishchenko, M. I. and Travis, L. D.: Capabilities and limitations of a current FORTRAN implementation of the T-matrix
677 method for randomly oriented, rotationally symmetric scatterers, J. Quant. Spectrosc. Radiat. Transf., 60, 309–324,
678 https://doi.org/10.1016/S0022-4073(98)00008-9, 1998.

679 Mishchenko, M. I., Travis, L. D., Kahn, R. A., and West, R. A.: Modeling phase functions for dustlike tropospheric aerosols
680 using a shape mixture of randomly oriented polydisperse spheroids, J. Geophys. Res. Atmospheres, 102, 16831–16847,
681 https://doi.org/10.1029/96JD02110, 1997.

682 Mishchenko, M. I., Travis, L. D., and Lacis, A. A.: Scattering, Absorption, and Emission of Light by Small Particles,
683 Cambridge University Press, 492 pp., 2002.

684 Mishchenko, M. I., Liu, L., and Videen, G.: Conditions of applicability of the single-scattering approximation, Opt. Express,
685 15, 7522, https://doi.org/10.1364/OE.15.007522, 2007.

686 Monge, M. E., Rosenørn, T., Favez, O., Müller, M., Adler, G., Abo Riziq, A., Rudich, Y., Herrmann, H., George, C., and
687 D'Anna, B.: Alternative pathway for atmospheric particles growth, Proc. Natl. Acad. Sci., 109, 6840–6844,
688 https://doi.org/10.1073/pnas.1120593109, 2012.

689 Müller, D., Veselovskii, I., Kolgotin, A., Tesche, M., Ansmann, A., and Dubovik, O.: Vertical profiles of pure dust and mixed
690 smoke–dust plumes inferred from inversion of multiwavelength Raman/polarization lidar data and comparison to AERONET
691 retrievals and in situ observations, Appl. Opt., 52, 3178, https://doi.org/10.1364/AO.52.003178, 2013.

692 Nousiainen, T.: Optical modeling of mineral dust particles: A review, J. Quant. Spectrosc. Radiat. Transf., 110, 1261–1279,
693 https://doi.org/10.1016/j.jqsrt.2009.03.002, 2009.

694 Ryder, C. L., Highwood, E. J., Rosenberg, P. D., Trembath, J., Brooke, J. K., Bart, M., Dean, A., Crosier, J., Dorsey, J.,
695 Brindley, H., Banks, J., Marsham, J. H., McQuaid, J. B., Sodemann, H., and Washington, R.: Optical properties of Saharan
696 dust aerosol and contribution from the coarse mode as measured during the Fennec 2011 aircraft campaign, Atmospheric
697 Chem. Phys., 13, 303–325, https://doi.org/10.5194/acp-13-303-2013, 2013.

698 Ryder, C. L., Highwood, E. J., Walser, A., Seibert, P., Philipp, A., and Weinzierl, B.: Coarse and giant particles are ubiquitous
699 in Saharan dust export regions and are radiatively significant over the Sahara, Atmospheric Chem. Phys., 19, 15353–15376,
700 https://doi.org/10.5194/acp-19-15353-2019, 2019.

701 Sakai, T., Nagai, T., Zaizen, Y., and Mano, Y.: Backscattering linear depolarization ratio measurements of mineral, sea-salt,
702 and ammonium sulfate particles simulated in a laboratory chamber, Appl. Opt., 49, 4441–4449,
703 https://doi.org/10.1364/AO.49.004441, 2010.

704 Scanza, R. A., Mahowald, N., Ghan, S., Zender, C. S., Kok, J. F., Liu, X., Zhang, Y., and Albani, S.: Modeling dust as
705 component minerals in the Community Atmosphere Model: development of framework and impact on radiative forcing,
706 Atmospheric Chem. Phys., 15, 537–561, https://doi.org/10.5194/acp-15-537-2015, 2015.

707 Schnaiter, M., Büttner, S., Möhler, O., Skrotzki, J., Vragel, M., and Wagner, R.: Influence of particle size and shape on the
708 backscattering linear depolarisation ratio of small ice crystals-cloud chamber measurements in the context of contrail and cirrus
709 microphysics, Atmospheric Chem. Phys., 12, 10465–10484, https://doi.org/10.5194/acp-12-10465-2012, 2012.

710 Shurcliff, W. A.: Polarized Light: Production and Use, 1962.

711 Sugimoto, N. and Lee, C. H.: Characteristics of dust aerosols inferred from lidar depolarization measurements at two
712 wavelengths, Appl. Opt., 45, 7468–7474, https://doi.org/10.1364/AO.45.007468, 2006.

713 Tesche, M., Ansmann, A., Müller, D., Althausen, D., Engelmann, R., Freudenthaler, V., and Groß, S.: Vertically resolved
714 separation of dust and smoke over Cape Verde using multiwavelength Raman and polarization lidars during Saharan Mineral
715 Dust Experiment 2008, J. Geophys. Res., 114, https://doi.org/10.1029/2009JD011862, 2009.

716 Tesche, M., Kolgotin, A., Haarig, M., Burton, S. P., Ferrare, R. A., Hostetler, C. A., and Mueller, D.: 3+2 + X: what is the
717 most useful depolarization input for retrieving microphysical properties of non-spherical particles from lidar measurements
718 using the spheroid model of Dubovik et al. (2006)?, 2019.

719 Weinzierl, B., Ansmann, A., Prospero, J. M., Althausen, D., Benker, N., Chouza, F., Dollner, M., Farrell, D., Fomba, W. K.,
720 Freudenthaler, V., Gasteiger, J., Groß, S., Haarig, M., Heinold, B., Kandler, K., Kristensen, T. B., Mayol-Bracero, O. L.,
721 Müller, T., Reitebuch, O., Sauer, D., Schäfler, A., Schepanski, K., Spanu, A., Tegen, I., Toledano, C., and Walser, A.: The
722 Saharan Aerosol Long-Range Transport and Aerosol–Cloud-Interaction Experiment: Overview and Selected Highlights, Bull.
723 Am. Meteorol. Soc., 98, 1427–1451, https://doi.org/10.1175/BAMS-D-15-00142.1, 2017.

724 Winker, D. M., Vaughan, M. A., Omar, A., Hu, Y., Powell, K. A., Liu, Z., Hunt, W. H., and Young, S. A.: Overview of the
725 CALIPSO Mission and CALIOP Data Processing Algorithms, J. Atmospheric Ocean. Technol., 26, 2310–2323,
726 https://doi.org/10.1175/2009JTECHA1281.1, 2009.

727 Wiscombe, W. J. and Mugnai, A.: Single scattering from nonspherical Chebyshev particles: a compendium of calculations,
728 1986.

729 Zong, R., Weng, F., Bi, L., Lin, X., Rao, C., and Li, W.: Impact of hematite on dust absorption at wavelengths ranging from
730 0.2 to 1.0 μm: an evaluation of literature data using the T-matrix method, Opt. Express, 29, 17405–17427,
731 https://doi.org/10.1364/OE.427611, 2021.

732   Zubko, E., Muinonen, K., Muñoz, O., Nousiainen, T., Shkuratov, Y., Sun, W., and Videen, G.: Light scattering by feldspar
733   particles: Comparison of model agglomerate debris particles with laboratory samples, J. Quant. Spectrosc. Radiat. Transf.,
734   131, 175–187, https://doi.org/10.1016/j.jqsrt.2013.01.017, 2013.

735